

## Turbulent diffusion in the geostrophic inverse cascade

By K. S. SMITH, G. BOCCALETTI, C. C. HENNING,  
I. MARINOV, C. Y. TAM, I. M. HELD AND G. K. VALLIS

GFDL/Princeton University, Princeton, NJ 08544, USA

(Received 28 August 2001 and in revised form 6 May 2002)

Motivated in part by the problem of large-scale lateral turbulent heat transport in the Earth's atmosphere and oceans, and in part by the problem of turbulent transport itself, we seek to better understand the transport of a passive tracer advected by various types of fully developed two-dimensional turbulence. The types of turbulence considered correspond to various relationships between the streamfunction and the advected field. Each type of turbulence considered possesses two quadratic invariants and each can develop an inverse cascade. These cascades can be modified or halted, for example, by friction, a background vorticity gradient or a mean temperature gradient. We focus on three physically realizable cases: classical two-dimensional turbulence, surface quasi-geostrophic turbulence, and shallow-water quasi-geostrophic turbulence at scales large compared to the radius of deformation. In each model we assume that tracer variance is maintained by a large-scale mean tracer gradient while turbulent energy is produced at small scales via random forcing, and dissipated by linear drag. We predict the spectral shapes, eddy scales and equilibrated energies resulting from the inverse cascades, and use the expected velocity and length scales to predict integrated tracer fluxes.

When linear drag halts the cascade, the resulting diffusivities are decreasing functions of the drag coefficient, but with different dependences for each case. When  $\beta$  is significant, we find a clear distinction between the tracer mixing scale, which depends on  $\beta$  but is nearly independent of drag, and the energy-containing (or jet) scale, set by a combination of the drag coefficient and  $\beta$ . Our predictions are tested via high-resolution spectral simulations. We find in all cases that the passive scalar is diffused down-gradient with a diffusion coefficient that is well-predicted from estimates of mixing length and velocity scale obtained from turbulence phenomenology.

---

### 1. Introduction

This paper is concerned with the problem of transport of a passive tracer in a turbulent flow. In addition to its intrinsic interest, the problem is relevant to the issue of meridional heat transport in the Earth's atmosphere and oceans. In mid-latitudes much of the atmospheric transport is effected by large-scale eddies that are well-described by the quasi-geostrophic equations of motion (e.g. Pedlosky 1987). In the classical two-layer model of geostrophic turbulence (e.g. Rhines 1977; Salmon 1980), at scales larger than the deformation radius the baroclinic streamfunction is nearly passively advected by the barotropic streamfunction, resulting in a down-scale cascade of its variance. But energy in the barotropic mode itself cascades to large scales. Since temperature is proportional to the baroclinic streamfunction, its nearly

passive advection by the barotropic flow determines the heat transport, and this down-gradient flux of heat in turn determines the extraction of energy from the mean flow (Larichev & Held 1995). To understand the heat transport properties of this system we must at least, then, understand the transport properties of a passive tracer being advected by a turbulent flow in which energy is cascading to larger scales, and that is the subject of this paper.

A familiar setting in which to explore this problem is that of conventional two-dimensional turbulence (see e.g. Kraichnan & Montgomery 1980; Vallis 1993; Danilov & Gurarie 2000 for reviews). In such flows, vorticity  $\zeta$  is advected by a flow defined by a streamfunction  $\psi$  linked to the vorticity, in Fourier transform space, by  $\zeta = -|\mathbf{k}|^2\psi$ . We will find it useful to consider more general relationships between streamfunction and advected field of the form  $\zeta = -|\mathbf{k}|^\alpha\psi$ . This is not only a formal device, for a number of physical systems can be realized by different choices of  $\alpha$ . For example, in surface quasi-geostrophic dynamics (e.g. Held *et al.* 1995), streamfunction  $\psi$  and advected quantity  $\zeta$  are related by  $\zeta = -|\mathbf{k}|\psi$ , and the equations represent the advection of temperature along a surface bounding a constant potential vorticity interior, so providing (for example) a simple model for edge waves on the tropopause or temperature advection near the Earth's surface. Large-scale quasi-geostrophic flow (quasi-geostrophic dynamics at scales large compared to the radius of deformation), may be a particularly useful model for Jovian dynamics, presuming that small-scale convection constitutes a source of turbulent energy. The latter case corresponds to, as we will see, yet a third relationship between advected scalar and associated streamfunction.

The dynamics of such generalized two-dimensional turbulence was explored by Pierrehumbert, Held & Swanson (1994) and Schorghofer (2000) with an emphasis on the forward cascade properties of the flow. Our focus is on the inverse cascade and the transport of a passive tracer by such flows. Thus, we consider fluids that are stirred at small scales by a random forcing, generating an inverse cascade, and which advect a passive tracer whose variance is maintained by a large-scale gradient. Most of the transport of the tracer thus occurs at scales within the inverse cascade of the turbulent fluid, just as for heat transport in baroclinic turbulence. We derive general expressions for the spectral shape of the inverse cascade in the presence of friction, as well as estimates of the halting scale, equilibrated energy level and tracer diffusivity. We then test these expressions numerically for the three cases of geostrophic turbulence mentioned above—conventional two-dimensional vorticity dynamics, surface quasi-geostrophic dynamics, and large-scale quasi-geostrophic dynamics—each of which has a different relationship between streamfunction and advected scalar. In conventional two-dimensional turbulence we also explore the effects of differential rotation, and we will see that the stopping scale of the inverse cascade is not necessarily the same as the mixing length of a passive scalar; we offer, and test, expressions for these two scales.

The theory presented in the paper is largely that of classical homogeneous turbulence, and accordingly we rely upon Kolmogorov–Kraichnan phenomenology, the presumption of well-defined eddy scales and magnitudes, and implicitly upon the convergence of flows to statistically steady states. Kolmogorov–Kraichnan phenomenology has been investigated for two-dimensional flows by many authors, and is generally found to hold best for flows that are largely free of coherent structures and devoid of intermittency. Examples of this can be found in, e.g. Maltrud & Vallis (1991) and Sukoriansky, Galperin & Chekhlov (1999) for the inverse cascade and Oetzel & Vallis (1997) and (at much higher resolution) Lindborg & Alvelius (2000) for the direct cascade. In the simulations we present, the flows are forced by small-

scale random noise, which appears to minimize the production of coherent vortices in the inverse cascade of standard two-dimensional turbulence. Moreover the inverse cascade is, in all cases, halted before the up-scale cascading invariant reaches the domain scale, preventing vortex condensation (Smith & Yakhov 1993). Nevertheless, in some cases investigated, coherent structures do form, and we will point out where these deviations from phenomenology occur.

Such phenomenology is sometimes questioned in the light of simulations of two-dimensional turbulence forced at small scales reported by Borue (1994). In those simulations it is found that while after a few eddy turn-around times the energy spectrum possesses a  $-5/3$  slope, at much later times the spectrum evolves to a  $-3$  slope, accompanied by coherent vortices in the flow. However, Borue employed an inverse hyper-viscosity (or ‘hypo’-viscosity) to absorb energy at large scales, rather than the more traditional and geophysically relevant linear drag. The former method of energy dissipation has recently been shown (Danilov & Gurarie 2001) to cause the steepening of the energy spectrum in the inverse cascade observed by Borue, while linear drag merely tapers the  $-5/3$  spectrum at large scales, so long as the drag is large enough to prevent significant energy from reaching the domain scale.

The paper is organized as follows. In §2 we introduce the basic formalism of generalized two-dimensional turbulence, and in §3 we discuss the fundamental spectral properties of such flows and calculate their corresponding inertial-range spectra using Kolmogorov–Kraichnan phenomenology. The dynamics of a passive tracer in an inverse cascade of generalized two-dimensional turbulence are discussed in §4. In §5 we heuristically derive a shape for the spectrum of the inverse cascade in the presence of drag, which in turn yields an estimate of the halting scale of the cascade. In §6 we add to the picture a mean vorticity gradient (the  $\beta$ -effect). This produces zonal jets, and we suggest expressions for both the jet scale and the eddy mixing scale. Finally, in §7, we report on numerical tests of our scaling predictions, and conclude in §8. An argument for cascade directions is given in Appendix A and some details of the numerical model are relegated to Appendix B.

## 2. Two-dimensional flow: a generalized formalism

Consider the two-dimensional advection equation for a conserved scalar field  $\xi$

$$\frac{\partial \xi}{\partial t} + J(\psi, \xi) = 0, \quad (2.1)$$

where  $\psi$  is the advecting streamfunction and  $J(A, B) = \partial_x A \partial_y B - \partial_y A \partial_x B$  is the Jacobian operator. The fluid velocity is given by  $\mathbf{u} = \hat{k} \times \nabla \psi$ .

In ordinary two-dimensional turbulence  $\xi = \nabla^2 \psi$ . Restricting attention to a doubly periodic domain, in Fourier transform space, this is equivalent to the relationship between Fourier components

$$\xi_k = -k^2 \psi_k, \quad (2.2)$$

where  $k = |\mathbf{k}|$  is the isotropic two-dimensional wavenumber. More generally we can consider the relationship between  $\xi_k$  and  $\psi_k$  discussed by Pierrehumbert *et al.* (1994),

$$\xi_k = -k^\alpha \psi_k, \quad (2.3)$$

where  $\xi$  will be referred to as the generalized vorticity field. The independent variables  $x, y$  have units of length  $[L]$ , and  $t$  has units of time  $[T]$ . Therefore, in order for

(2.1) to be dimensionally balanced,  $\psi \sim [L^2 T^{-1}]$  and  $\xi \sim [L^{2-\alpha} T^{-1}]$ . Three particular values of  $\alpha$  lead to geophysically relevant equations:  $\alpha = 2$ ,  $\alpha = 1$  and  $\alpha = -2$ .

$\alpha = 2$ : *Two-dimensional vorticity dynamics*

If  $\alpha = 2$  we obtain the familiar two-dimensional Euler, or barotropic vorticity equation, with  $\xi = \zeta$  and  $\zeta \sim [T^{-1}]$ . In this paper we shall refer to these dynamics as two-dimensional vorticity (TDV) dynamics.

$\alpha = 1$ : *Surface quasi-geostrophic dynamics*

When  $\alpha = 1$  we obtain surface quasi-geostrophic (SQG) dynamics (e.g. Held *et al.* 1995, and references therein). These equations describe the evolution of surface temperature perturbations bounding a constant potential vorticity interior, within the quasi-geostrophic equations.

$\alpha = -2$ : *Large-scale quasi-geostrophic dynamics*

The case  $\alpha = -2$  corresponds to a rescaled shallow-water quasi-geostrophic equation in the asymptotic limit of length scales large compared to the deformation scale (this system was investigated by Larichev & McWilliams 1991). We term this type of flow *large-scale quasi-geostrophic (LQG) dynamics*. Consider the shallow-water quasi-geostrophic equations

$$\frac{\partial q}{\partial t} + J(\psi, q) = 0, \quad q = (\nabla^2 - \lambda^2)\psi, \quad (2.4)$$

where  $\lambda$  is the deformation wavenumber. In Fourier space the expression for the potential vorticity  $q$  is

$$q_k = -(k^2 + \lambda^2)\psi_k. \quad (2.5)$$

For wavenumbers such that  $k \gg \lambda$ , we recover TDV, but when  $k \ll \lambda$ , (2.4) becomes

$$-\lambda^2 \frac{\partial \psi}{\partial t} + J(\psi, \nabla^2 \psi) = 0. \quad (2.6)$$

Because  $\lambda$  only appears in combination with the time derivative, we can rescale time

$$\tau = t\lambda^{-2}, \quad (2.7)$$

and make the substitution of variables

$$\xi = \psi \quad \text{and} \quad \Psi = \nabla^2 \psi \quad (2.8)$$

so that (2.6) becomes

$$\frac{\partial \xi}{\partial \tau} + J(\Psi, \xi) = 0, \quad \Psi = \nabla^2 \xi. \quad (2.9)$$

In Fourier space the relation between  $\xi$  and  $\Psi$  is

$$\xi_k = k^{-2}\Psi_k \quad (2.10)$$

which has the same form as (2.3) with  $\alpha = -2$ .

Nonlinear advection is present in all of these geophysical cases, thus turbulence and turbulent cascades can develop. The character of the turbulence – e.g. the spectral shapes, eddy scales, cascade directions, statistical amplitudes, coherent structures and rates of turbulent development – will be distinct in each case. Some aspects of these distinctions were discussed by Pierrehumbert *et al.* (1994), who argued, for example, that the enstrophy cascade should be dominated by local strain for  $\alpha < 2$ , and that

local scaling predictions should break down for  $\alpha > 2$ . Furthermore, they note that the inverse cascade—our primary concern in this paper—should remain local for all  $\alpha < 4$ ; the three cases discussed above fall into this category.

The fact that a single generalized formalism describes three cases of geophysical interest by changing the value of a single parameter provides strong motivation in itself to investigate the properties of the general system. We may also regard the generalized turbulence formalism, however, as a shorthand with which we can derive common aspects of the flows without repetition.

In order to make quantitative statements about scales and energies (a necessary prerequisite to predicting the statistics of passive tracer advection) we first consider the Kolmogorov spectra for the generalized dynamics. Some of what follows in the next section was derived by Pierrehumbert *et al.* (1994), but we include it for clarity, notation and as a reference basis for the rest of the paper.

### 3. Spectral properties of generalized two-dimensional flow

Because  $\xi$  is conserved on parcels, the integral over a periodic domain (or an enclosed domain with no-normal-flow boundary conditions) of any function of  $\xi$  is conserved. Thus, there are an infinite number of invariants. However, just as for TDV flow, two quadratic invariants determine the cascade directions. From (2.1) these are

$$E_G \equiv -\frac{1}{2}\overline{\psi\xi}, \quad Z_G \equiv \frac{1}{2}\overline{\xi^2}, \quad (3.1)$$

where the overline indicates a horizontal average. We will refer to  $E_G$  as the generalized energy, and to  $Z_G$  as the generalized enstrophy. The invariants have units  $E_G \sim [L^{4-\alpha}T^{-2}]$  and  $Z_G \sim [L^{4-2\alpha}T^{-2}]$ . (Note that for LQG,  $T$  is the rescaled time from (2.7).) The spectra of the two quadratic invariants are connected by a simple relationship involving scale only. To see this, we define the isotropic spectra  $\mathcal{A}(k)$  of the positive definite quantity  $A$  such that

$$A = \int_0^\infty \mathcal{A}(k) dk, \quad (3.2)$$

where  $k$  is the isotropic wavenumber, and  $\mathcal{A}(k)$  is either  $\mathcal{E}_G(k)$  or  $\mathcal{Z}_G(k)$  (thus the dimensions of  $\mathcal{E}_G(k) \sim [L][E_G]$  and  $\mathcal{Z}_G(k) \sim [L][Z_G]$ ). The coupling relationship (2.3), together with Parseval's theorem, implies that

$$\mathcal{Z}_G(k) = k^\alpha \mathcal{E}_G(k). \quad (3.3)$$

Well-known arguments (Batchelor 1953) lead one to expect that, in TDV flow, energy will cascade to larger scale and enstrophy will cascade to smaller scale. These arguments are based on the presumption that the distribution of the spectra of each invariant spreads in wavenumber space. In Appendix A we extend such arguments to the case with arbitrary  $\alpha$  and show that, for  $\alpha > 0$ , generalized energy cascades to larger scale and generalized enstrophy cascades to smaller scales. For  $\alpha < 0$ , however, it turns out that generalized energy cascades to *small* scales, and generalized enstrophy cascades to *large* scale.

If there is a spectrally localized source of variance of  $E_G$  and  $Z_G$ , then in all the above cases we expect there will be a transfer of generalized energy and generalized enstrophy in opposite directions, away from the source region, just as in TDV dynamics. If frictional effects only act at some spectral distance from the source then we might expect inertial ranges to form between source and sink. If this is the case one can derive the spectral slopes of these putative inertial ranges.

Between source and sink the spectral flux  $\varepsilon_E$  or  $\varepsilon_Z$  associated with the generalized energy or enstrophy will be constant, producing an inertial range. We assume that over their respective inertial ranges, the local spectral density  $\mathcal{E}_G(k)$  and  $\mathcal{Z}_G(k)$  are functions only of the local spectral flux of  $E_G$  or  $Z_G$  and of the scale itself—the locality hypothesis of Kolmogorov (1941). Thus

$$\varepsilon_A = \frac{k\mathcal{A}(k)}{T_A(k)} = \text{constant}, \quad (3.4)$$

where  $A$  is  $E_G$  or  $Z_G$  and  $T_A(k)$  is a local timescale. From dimensional considerations

$$T_E(k) = [k^{5-\alpha}\mathcal{E}_G(k)]^{-1/2}, \quad (3.5a)$$

$$T_Z(k) = [k^{5-2\alpha}\mathcal{Z}_G(k)]^{-1/2}. \quad (3.5b)$$

Using the expression for the flux (3.4) we obtain

$$\mathcal{E}_G(k) = \mathcal{C}_E \varepsilon_E^{2/3} k^{(\alpha-7)/3}, \quad (3.6a)$$

$$\mathcal{Z}_G(k) = \mathcal{C}_Z \varepsilon_Z^{2/3} k^{(2\alpha-7)/3}, \quad (3.6b)$$

where  $\mathcal{C}_E$  and  $\mathcal{C}_Z$  are the Kolmogorov constants for the respective cascades of  $E_G$  and  $Z_G$ . Because the dynamics for each type of turbulence are different,  $\mathcal{C}_E$  and  $\mathcal{C}_Z$  can depend on  $\alpha$ . Note also that one can find the spectrum  $\mathcal{Z}_G(k)$  in the  $E_G$ -range or  $\mathcal{E}_G(k)$  in the  $Z_G$ -range via (3.3).

As a useful shorthand, we combine these results by writing the spectrum of a generalized invariant as

$$\mathcal{A}(k) = \mathcal{C} \varepsilon^{2/3} k^{-\gamma}, \quad (3.7)$$

where the exponent  $\gamma$  is

$$\gamma = \begin{cases} (7-\alpha)/3, & A = E_G \\ (7-2\alpha)/3, & A = Z_G. \end{cases} \quad (3.8)$$

Note that as defined,  $\gamma \geq 1$  for all cases considered in this paper. For future reference, using (3.4) and (3.7), the generalized eddy timescale is then

$$T_A(k) = [k^{3\gamma-2}\mathcal{A}(k)]^{-1/2} = \mathcal{C}^{-1/2} \varepsilon^{-1/3} k^{1-\gamma}. \quad (3.9)$$

Schema of the expected cascade directions and spectral slopes for each of the three cases considered in this paper can be found in figure 1. Also noted are the dimensional estimates of the linear drag-induced stopping scale (discussed in §5), and the spectra of the velocity variance  $\mathcal{E}$  for each case. The latter is necessary since r.m.s. velocities will be needed to predict diffusivities in §4. In order to calculate the spectral slope of the velocity variance one must multiply  $\mathcal{A}(k)$ , the upscale cascading invariant, by the power of  $k$  necessary to give a spectrum with dimensions  $[L^3 T^{-2}]$ , a power which varies from case to case since  $\mathcal{A}(k)$  has dimensions which depend on  $\alpha$ . One must be careful in the LQG case, since in this case time has been re-dimensioned via (2.7). Particulars of the velocity estimates will be addressed for each case separately as necessary in the context of the numerical calculations discussed in §7.

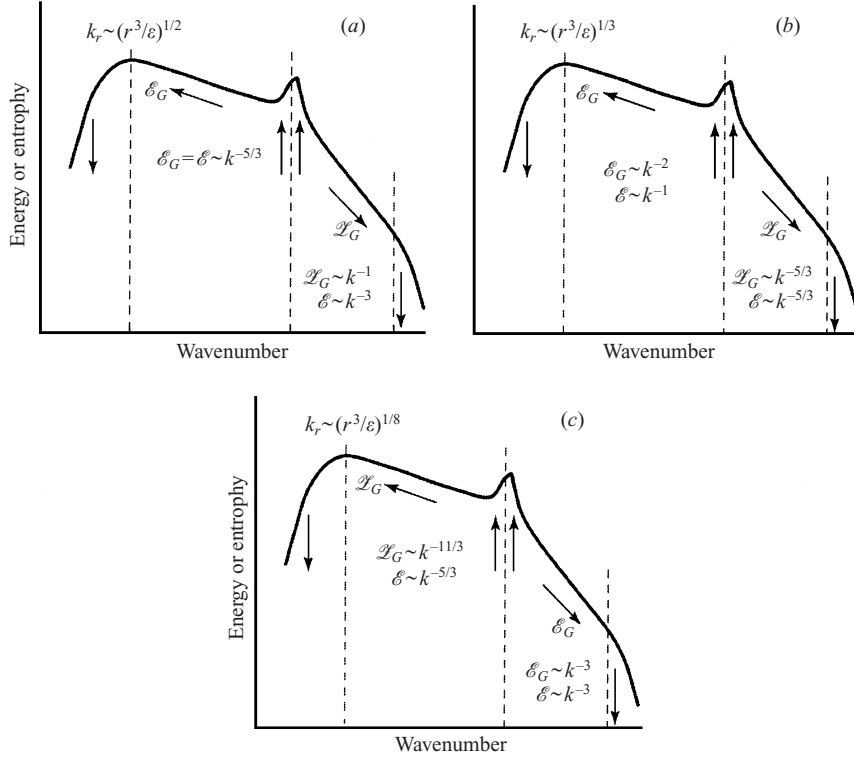


FIGURE 1. Schematic diagram of the cascades in (a) two-dimensional vorticity dynamics, (b) surface quasi-geostrophic dynamics, and (c) large-scale quasi-geostrophic dynamics. Each panel indicates the cascade directions, the spectrum of each cascading invariant in its own inertial range ( $\mathcal{E}_G$  or  $\mathcal{Z}_G$ ), the spectrum of the velocity variance ( $\mathcal{E}$ ), and the dimensional estimate of the scale at which the inverse cascade is halted by linear drag,  $k_r$ . The upward arrows represent the injection of the invariants while the downward arrows represent their dissipation.

#### 4. Passive tracer dynamics

Suppose now that the streamfunction  $\psi$  determined by the advection equation (2.1) and the coupling (2.3) also advects a passive tracer  $\phi$ , for which the equation is

$$\frac{\partial \phi}{\partial t} + J(\psi, \phi) = \mathcal{D}_\phi, \quad (4.1)$$

where  $\mathcal{D}_\phi$  represents dissipation, presumed to occur at small scales. (In the LQG case, the streamfunction advecting the tracer is the QG streamfunction  $\psi$ , which determines the velocities, rather than the redefined streamfunction of (2.8).) The tracer variance

$$P \equiv \frac{1}{2} \overline{\phi^2} \quad (4.2)$$

is a conserved quantity of the tracer field in the absence of dissipation. In the inertial range of  $A$ —some conserved quantity of the flow field—the spectral flux  $\chi$  of tracer variance is

$$\chi = \frac{k \mathcal{P}(k)}{T_E(k)} = \text{constant}, \quad (4.3)$$

where  $\mathcal{P}(k)$  is the spectrum of the tracer variance and  $T_E(k)$  is the timescale associated with the kinetic energy in the inertial range of  $A$ . In general there is only one spectrally

local timescale available, namely (3.9). In this case the tracer variance spectrum is

$$\mathcal{P}(k) = \mathcal{K} \chi \varepsilon^{-1/3} k^{-\gamma}, \quad (4.4)$$

where  $\mathcal{K}$  is the Kolmogorov constant for the tracer. In general, then, the tracer variance follows the same power law as the spectrum of the advecting flow invariant, in that invariant's inertial range. For example, in the case  $\alpha = 2$  (TDV), tracer variance has the slope  $-5/3$  in the energy inertial range, and slope  $-1$  in the enstrophy inertial range.

When LQG describes the dynamics, however, these predictions should only hold if the tracer is advected by the redefined streamfunction. This is not the relevant physical situation. The variance of the tracer as given by (4.1) requires that we specify the timescale  $T_E(k)$  in terms of physical scales, which re-introduces the deformation scale into the calculation. The up-scale cascading invariant is then associated with the available potential energy (APE) and the direct cascading invariant is the kinetic energy (KE). The latter has a spectral slope of  $k^{-5/3}$  in the inertial range of the APE, yielding an expected tracer variance spectral slope of  $k^{-5/3}$  as well.

Suppose now that tracer variance is generated by the presence of a fixed large-scale meridional gradient and absorbed by small-scale dissipation. Specifically, we consider

$$\frac{\partial \phi}{\partial t} + J(\psi, \phi) + \bar{\theta} v = \mathcal{D}_\phi, \quad (4.5)$$

where  $v = \partial \psi / \partial x$  is the meridional velocity of the advecting flow and  $\bar{\theta} \equiv \partial \bar{\phi} / \partial y$  is the mean tracer gradient. Since (4.5) is linear in  $\phi$ , we can rescale the equation such that  $\bar{\theta} = 1$ . Multiplying (4.5) by  $-\phi$  and averaging over space yields

$$\frac{dP}{dt} = \overline{\phi v} - \overline{\phi \mathcal{D}_\phi}, \quad (4.6)$$

where  $P$  is the tracer variance of (4.2). The meridional flux of tracer is the explicit source of variance in the tracer field, and can be written

$$\overline{\phi v} = -D, \quad (4.7)$$

where  $D$  is the diffusivity, which has dimensions  $[L^2 T^{-1}] = [VL]$ . If the advecting meridional velocity field is sharply peaked at some scale  $k_0$  and has a r.m.s. value  $V_{rms}$ , then a standard downgradient mixing hypothesis (e.g. Tennekes & Lumley 1994, chap. 8) yields an expected diffusivity

$$D \simeq V_{rms} k_0^{-1}. \quad (4.8)$$

One can make a crude estimate of the tracer flux spectrum by decomposing the left-hand side of (4.7) and estimating the two fields separately, yielding

$$\mathcal{D}(k) \sim \mathcal{E}^{1/2}(k) \mathcal{P}^{1/2}(k), \quad (4.9)$$

We shall derive specific diffusivity estimates for each of our cases and test their accuracy numerically. In order to do so, however, we must first derive estimates for  $k_0$  and  $V_{rms}$ .

## 5. Cascade reduction by linear drag

An inverse cascade will be diminished or halted when the up-scale-cascading invariant either reaches the domain scale, or the scale at which some competing process such as friction dominates nonlinear advection. If some mechanism halts the

cascade of whichever invariant is cascading up-scale at wavenumber  $k_0$ , and if the eddies are forced at wavenumber  $k_f$ , then we must presume that

$$k_f > k_0. \quad (5.1)$$

If the spread between these scales is large, an inertial range may exist between them.

As the eddies cascading through the system become larger, they also become slower. In particular, we presume an eddy timescale given by (3.9). If the mechanism competing against nonlinear advection has a timescale ( $T_{halt}$ ) that is independent of scale, or increases less rapidly than  $T_{eddy}$  with increasing scale, then at some point in the cascade,  $T_{eddy} \sim T_{halt}$ . This expression can presumably be used to find the scale  $k_0$  at which the cascade is halted, analogous to the derivation of the Kolmogorov micro-scale at which molecular viscosity overcomes the direct cascade.

Consider the case of a linear vorticity drag with the equation of motion

$$\frac{\partial \xi}{\partial t} + J(\psi, \xi) = F - r\xi, \quad (5.2)$$

where  $F$  is the forcing. Physically, the term  $r\xi$  represents a drag due to Ekman friction in TDV, or thermal damping in SQG or LQG. Note that  $r \sim [T^{-1}]$ : the drag coefficient has dimensions of an inverse time for all couplings  $\alpha$ . For TDV with linear drag, Arbic (2000, p. 122) proves that (5.1) must hold for all values of drag coefficient.

If the time-averaged generalized energy (enstrophy) injection rate  $g$  is known and  $\alpha > 0$  ( $\alpha < 0$ ), the equilibrated generalized energy (enstrophy) level can be calculated exactly. To see this, multiply (5.2) by  $-\psi(-\xi)$  and integrate over space to form the generalized energy (enstrophy) budget equation

$$A = g - 2rA, \quad (5.3)$$

where  $g$  is the generation rate

$$g = \begin{cases} -\overline{\psi F}, & \alpha > 0 \\ -\overline{\xi F}, & \alpha < 0. \end{cases} \quad (5.4)$$

In steady state

$$A = A_r = \frac{g}{2r}, \quad (5.5)$$

thus we know in advance the total generalized energy (enstrophy) of the statistically steady flow for  $\alpha > 0$  ( $\alpha < 0$ ). We have neglected the effects of small-scale dissipation in the above calculation, but in the time-average, small-scale dissipation simply decreases the net generation rate by a calculable amount. This will be discussed further in the context of the numerical simulations.

### 5.1. Dimensional estimates of halting scale

Using (3.9), setting  $T_A = r^{-1}$  and assuming  $g = \varepsilon$  gives an estimate for the halting scale:

$$k_r \sim (r^3 g^{-1})^{1/[3(\gamma-1)]}. \quad (5.6)$$

For our three special cases this yields

$$\text{TDV: } k_r \sim (r^3 g^{-1})^{1/2}, \quad (5.7a)$$

$$\text{SQG: } k_r \sim (r^3 g^{-1})^{1/3}, \quad (5.7b)$$

$$\text{LQG: } k_r \sim (r^3 g^{-1})^{1/8}, \quad (5.7c)$$

where  $g$  is the injection rate of the appropriate up-scale-cascading invariant.

The expression (5.6) is demanded by dimensional consistency, and so gives no indication of the value of any numerical prefactor. One simple way to derive such a prefactor is to note that the integral of the energy spectrum (3.7) must be consistent with the total energy as given by (5.5). That is,

$$\int_{k_r}^{\infty} \mathcal{C} \varepsilon^{2/3} k^{-\gamma} dk = \frac{g}{2r}, \quad (5.8)$$

where we have assumed that the energy content in the larger scales ( $k < k_r$ ) is negligible. For  $\gamma > 1$  this gives

$$k_r \approx \left( \frac{2\mathcal{C}}{\gamma - 1} \right)^{1/(\gamma-1)} (r^3 g^{-1})^{1/[3(\gamma-1)]}, \quad (5.9)$$

which is identical to (5.6), except for the numerical coefficient involving the Kolmogorov constant. For TDV, this gives

$$k_r \approx (3\mathcal{C})^{3/2} (r^3 g^{-1})^{1/2}. \quad (5.10)$$

Danilov & Gurarie (2001) independently proposed an identical scaling. This coefficient is accurate only to the extent that the energy falls off very rapidly for wavenumbers smaller than  $k_r$ .

## 5.2. Spectral shapes

By making one additional assumption, we can derive an expression for the spectral shape that is putatively valid in the inertial range and in the range where friction begins to dominate. The peak of this theoretical spectrum, derived in a manner similar to that of Leith (1967) and Lilly (1972), yields a better estimate for the stopping-scale prefactor than (5.9). However, we only expect the theory to be relevant in parameter regimes such that the underlying inertial range is present and free of intermittency, and make no claim that the derived spectral shape is universal.

The spectral budget equation for generalized energy (enstrophy) in mode  $\mathbf{k}$  for  $\alpha > 0$  ( $\alpha < 0$ ) is

$$\frac{\partial A_{\mathbf{k}}}{\partial t} = \varepsilon_{\mathbf{k}} - 2rA_{\mathbf{k}} + g\delta(k - k_f), \quad (5.11)$$

where  $A_{\mathbf{k}} = |\psi_{\mathbf{k}}|^2/2$  (or  $\text{Re}[\zeta_{\mathbf{k}}^* \psi_{\mathbf{k}}]/2$ ),  $\varepsilon_{\mathbf{k}}$  is the transfer rate at  $\mathbf{k}$  arising from the real part of the product of  $-\psi_{\mathbf{k}}^*$  and the spectral Jacobian term, and  $g$  is the generalized energy (enstrophy) injection, localized at isotropic wavenumber  $k_f$ . We assume a steady state, so that the time derivative vanishes, and isotropy so that  $\mathbf{k}$  can be replaced by  $k$ . If the source term is at some high wavenumber  $k_f \gg k_r$  then we may expect an inverse cascade initially unfettered by friction. At smaller wavenumbers, the drag will remove energy from the flow, and, without further approximation, the spectral transfer is governed by the budget equation

$$\frac{d\varepsilon}{dk} = 2r\mathcal{A}(k). \quad (5.12)$$

That is, the energy flux is reduced by the frictional loss.

We now assume that the spectrum (3.7) can be substituted for  $\mathcal{A}(k)$ , but let  $\varepsilon = \varepsilon(k)$  therein. This is a perturbative solution for small drag-induced deviations from the inertial-range flux. Thus we expect the approximation to be valid in the spectral regions where drag is small and up to the scales where it begins to dominate, but not

at the frictionally dominated, largest scales. In this approximation (5.12) becomes

$$\frac{d\varepsilon}{dk} = 2r\mathcal{C}\varepsilon^{2/3}k^{-\gamma}, \quad (5.13)$$

which readily yields

$$\varepsilon(k) = \left[ \frac{2\mathcal{C}}{3(1-\gamma)}rk^{1-\gamma} + c \right]^3, \quad (5.14)$$

where  $c$  is the integration constant. The transfer rate must be equal to the generation rate at the forcing scale, i.e.

$$\varepsilon(k_f) = g, \quad (5.15)$$

which we use to solve for the integration constant in (5.14). Using the solution for  $c$ , the flux is

$$\varepsilon(k) = g \left[ 1 - (k_c/k)^{\gamma-1} + (k_c/k_f)^{\gamma-1} \right]^3, \quad (5.16)$$

where

$$k_c = \left[ \frac{2\mathcal{C}}{3(\gamma-1)} \right]^{1/(\gamma-1)} (r^3 g^{-1})^{1/[3(\gamma-1)]}. \quad (5.17)$$

Substituting this into (3.7) gives us an estimate for the spectrum of the invariant in the presence of linear drag:

$$\mathcal{A}(k) = \mathcal{C}g^{2/3}k^{-\gamma} \left[ 1 - (k_c/k)^{\gamma-1} + (k_c/k_f)^{\gamma-1} \right]^2. \quad (5.18)$$

For TDV, the expression (5.18) in the limit  $k_f \rightarrow \infty$  was derived by Lilly (1972). The reader may verify that the expression for  $\mathcal{A}(k)$  satisfies

$$\int_{k_c}^{\infty} \mathcal{A}(k) dk = \frac{g}{2r} \quad (5.19)$$

exactly.

For  $k_f \gg k_c$ , the third term in brackets is small and can be neglected (but we shall retain it in our predictions for the simulated spectra). For wavenumbers  $k \gg k_c$ , the second term in square brackets in (5.18) is also negligible and the spectrum reduces to (3.7). For sufficiently small wavenumbers,  $\varepsilon(k)$  given by (5.16) is not positive. The critical wavenumber at which the spectral flux vanishes is  $k = k_c$  (assuming  $k_f \rightarrow \infty$ ), where  $k_c$  is given by (5.17). It is unphysical for  $\mathcal{A}(k)$  to vanish identically at some finite  $k$ . The weakness of this derivation is just the use of the inertial-range spectrum (3.7) in (5.12), an assumption we expect to be valid only if frictional effects are small perturbations on the inertial flow, as mentioned above.

The predicted spectral shapes for the three cases we consider here are (assuming  $k_f \rightarrow \infty$ )

$$\text{TDV: } \mathcal{E}(k) = \mathcal{C}g^{2/3}k^{-5/3} \left[ 1 - (k_c/k)^{2/3} \right]^2, \quad k_c = \mathcal{C}^{3/2}(r^3 g^{-1})^{1/2}, \quad (5.20a)$$

$$\text{SQG: } \mathcal{E}(k) = \mathcal{C}g^{2/3}k^{-2} \left[ 1 - (k_c/k) \right]^2, \quad k_c = (2\mathcal{C}/3)(r^3 g^{-1})^{1/3}, \quad (5.20b)$$

$$\text{LQG: } \mathcal{L}(k) = \mathcal{C}g^{2/3}k^{-11/3} \left[ 1 - (k_c/k)^{8/3} \right]^2, \quad k_c = (\mathcal{C}/4)^{3/8}(r^3 g^{-1})^{1/8}, \quad (5.20c)$$

where in each case the spectrum is valid for all  $k > k_c$ , and  $\mathcal{C}$  and  $g$  are the Kolmogorov constant and injection rate, respectively, for the particular dynamics at hand.

A quantitative estimate of the drag-induced halting scale can be made by calculating

the location of the peak wavenumber  $k_0 = k_r$  by setting

$$\left. \frac{d\mathcal{A}(k)}{dk} \right|_{k=k_r} = 0. \quad (5.21)$$

This yields

$$k_r = \Gamma (r^3 g^{-1})^{1/[3(\gamma-1)]}, \quad \Gamma = \left[ \frac{2\mathcal{C}(3\gamma-2)}{3\gamma(\gamma-1)} \right]^{1/(\gamma-1)}. \quad (5.22)$$

For our three cases, the drag-induced stopping scales expected are

$$\text{TDV: } k_r = (9\mathcal{C}/5)^{3/2} (r^3 g^{-1})^{1/2}, \quad (5.23a)$$

$$\text{SQG: } k_r = (4\mathcal{C}/3) (r^3 g^{-1})^{1/3}, \quad (5.23b)$$

$$\text{LQG: } k_r = (27\mathcal{C}/44)^{3/8} (r^3 g^{-1})^{1/8}. \quad (5.23c)$$

As in (5.10), the prefactor  $\Gamma$  in each case is not necessarily an order-unity quantity. In the case of energy in TDV turbulence, for example, using the estimate  $\mathcal{C} = 5.8$  (Maltrud & Vallis 1991) yields  $\Gamma = (9\mathcal{C}/5)^{3/2} = 33.7$ . Using (5.10) gives 72.6, the larger number being consistent with the assumption that energy is strictly zero for wavenumbers smaller than  $k_r$ . Our numerical results (discussed in §7) are consistent with these estimates; that is, the strictly dimensional estimate  $k_r = (r^3/g)^{1/2}$  is more than an order of magnitude smaller than the actual wavenumber at which the cascade is halted. The large value of  $\Gamma$  indicates that, in the presence of drag, TDV turbulence is more inefficient at moving energy to larger scales than one might expect from dimensional estimates alone.

## 6. Mean vorticity gradients: the $\beta$ -effect

In two-dimensional vorticity dynamics, a meridional gradient of planetary vorticity may be represented by the  $\beta$ -effect. In SQG, a meridional gradient of temperature gives rise to a similar term in the equation of motion. Including such effects in (5.2), we write

$$\frac{\partial \xi}{\partial t} + J(\psi, \xi) + \beta \frac{\partial \psi}{\partial x} = F - r\xi, \quad (6.1)$$

where we use the symbol  $\beta$  for the constant mean gradient of  $\xi$  with units  $\beta \sim [L^{1-\alpha} T^{-1}]$ . Because  $\beta$  introduces anisotropy into the dynamics (Rhines 1975; Vallis & Maltrud 1993), the halting scale, if present, will be anisotropic as well. However, the dual presence of  $\beta$  and  $r$  introduces complexities to the dynamics which, even for TDV, have only recently come to be appreciated (Chekhlov *et al.* 1996; Manfroi & Young 1999; Smith & Waleffe 1999; Huang, Galperin & Sukoriansky 2001; Galperin, Sukoriansky & Huang 2001; Danilov & Gryanik 2001). The mean vorticity gradient admits a possible tri-partite balance in the equation of motion between nonlinear advection, advection of the mean gradient (and thereby possible wave propagation) and dissipation.

We direct the discussion here to the two cases with  $\alpha > 0$ : TDV and SQG. The  $\beta$ -term as defined in (6.1) physically represents the Coriolis gradient in TDV, and a mean temperature gradient in SQG, but has no obvious physical interpretation for LQG†.

† Keeping the same definition of  $\beta$  as in TDV, we obtain a term of the form  $\beta \partial \xi / \partial x$  added to the left-hand side of (2.9). The dispersion relation is the same as that for equivalent barotropic Rossby waves at large scales, namely  $\omega_{RLQG} = -k_x \beta / \lambda^2$ . The frequency goes linearly to zero rather than diverging at large scale, hence it is not clear that  $\beta$  can halt the cascade in this case.

## 6.1. Waves, turbulence and drag

The first significant scale for these flows is determined by the balance between nonlinear advection and advection of the mean gradient. Ignoring drag for the moment, Rossby waves in the generalized two-dimensional formalism will have the dispersion relation

$$\omega_R = -\frac{k_x \beta}{k^\alpha}. \quad (6.2)$$

Following Vallis & Maltrud (1993) we set this equal to the eddy strain rate (the inverse of 3.9) to find the boundary between  $\beta$ -dominated and isotropic flow,

$$k(\theta) = k_\beta (\cos \theta)^{1/(\alpha+\gamma-2)} \quad (6.3)$$

where

$$k_\beta = (\mathcal{C}^{-1/2} \beta \varepsilon^{-1/3})^{1/(\alpha+\gamma-2)}. \quad (6.4)$$

Note that in the case of energy in TDV dynamics ( $\alpha = 2$  and  $\gamma = 5/3$ ), expression (6.4) becomes

$$k_\beta \simeq \left( \frac{\beta^3}{\mathcal{C}^{3/2} \varepsilon} \right)^{1/5}, \quad (6.5)$$

a form similar to that of Vallis & Maltrud (1993), apart from the non-dimensional factors in the denominator (which we keep for later use).

The relation (6.3) specifies a parametric relationship between the modulus of wavenumber  $k$  and the wave direction  $\theta = \arctan(k_y/k_x)$  having the shape of a dumbbell in the  $(k_x, k_y)$ -plane and having a maximum at  $\theta = 0$  (along the  $k_x$ -axis). Thus for  $\beta$  such that  $k_\beta \ll k_f$ , we expect an isotropic inverse cascade up to  $k_\beta$ , and anisotropic flow at wavenumbers below  $k_\beta$ , rather than a simple halting of the inverse cascade at  $k_\beta$ . Because weakly nonlinear wave interaction typical of anisotropic flows is not as efficient as isotropic turbulence at cascading the invariant, we expect this boundary to be significant also in the spectral distribution of energy. Along the  $k_y$  axis, (6.3) gives  $k(\theta = \pi/2) = 0$ . There is evidence (Vallis 1993; Chekhlov *et al.* 1996; Smith & Waleffe 1999; Huang *et al.* 2001) that energy (in TDV flow on the torus or sphere) will continue to cascade to larger scale past  $k_\beta$ , but with most of the energy concentrated along the  $k_y$ -axis.

When drag is present, and the drag coefficient  $r$  is sufficiently large, a balance can be reached between dissipation and nonlinear advection at scales smaller than those at which  $\beta$  becomes important, and the cascade is then halted isotropically. A critical value exists for  $r$ , separating the isotropic steady-state flow from one in which anisotropy is allowed to develop. This critical value of  $r$  is found by setting  $k_r = k_\beta$ , using (5.22) and (6.4), yielding

$$r_c = \Gamma^{1-\gamma} g^{(1-\alpha)/[3(2-\gamma-\alpha)]} (\mathcal{C}^{-1/2} \beta)^{(1-\gamma)/(2-\gamma-\alpha)}. \quad (6.6)$$

In the TDV case with  $\alpha = 2$  and  $\gamma = 5/3$  this expression gives

$$r_{c,\alpha=2} = \frac{5}{9\mathcal{C}} (\beta^2 g)^{1/5}. \quad (6.7)$$

In the rest of this discussion, we will assume that  $r < r_c$ , so that an anisotropic, large-scale spectrum should ensue. It then remains to determine the largest scale to which this anisotropic spectrum extends, and expecting this scale to depend on both  $\beta$  and  $r$ , we denote it  $k_{\beta,r}$ .

6.2. Estimates of the halting scale with  $\beta$  and drag present

For clarity of presentation we focus on TDV, and then discuss how it may be adapted to generalized two-dimensional turbulence. In the small-drag limit ( $r \ll r_c$ ) we seek an estimate for the halting scale  $k_{\beta,r}$ , that is for the scale at which the maximum energy is found. Because in anisotropic turbulence most of the energy goes into zonal jets it is not surprising that this estimate will be particularly apt as an estimate for the separation scale of the jets themselves. Our argument has two components: (i) the forcing and dissipation set the r.m.s. velocity; (ii) using this in conjunction with the  $\beta$ -effect provides an estimate of the halting scale. We shall see that despite the jet scale being the most energetic scale, it is the inviscid scale (6.4) that characterizes the meridional transport of passive tracer.

If one assumes that, at scales where  $\beta$  is important but where drag is not yet significant ( $k_{\beta,r} < k < k_\beta$ ), the spectral slope is a function only of  $\beta$  and wavenumber, then dimensional analysis leads to the expression

$$\mathcal{E}_\beta(k) = \mathcal{C}_\beta \beta^2 k^{-5}, \quad (6.8)$$

as pointed out by Rhines (1975). Obviously, though, the spectrum cannot be isotropic, since it is derived specifically in the region where anisotropy is present. Our simulations, as well as those of Galperin *et al.* (2001) and others cited above, demonstrate that at scales  $k_{\beta,r} < k < k_\beta$ , energy is concentrated along the  $k_x = 0$  axis, but does roughly follow a  $k^{-5}$  power law. Chekhlov *et al.* (1996) point out that energy continues to follow a  $k^{-5/3}$  power law for all wavenumbers  $k_{\beta,r} < k < k_\beta$  with  $k_x \neq 0$ , but that implies that modes with  $k_x \neq 0$  contribute negligibly to the total spectrum at large scale.

Chekhlov *et al.* (1996) and Smith & Waleffe (1999) discuss the subtleties of the transfer from the two-dimensional isotropic cascade to the one-dimensional ‘cascade’ along the zonal axis. If the energy is concentrated on the  $k_x = 0$  axis, precisely where the  $\beta$ -term in (6.1) vanishes, then the dependence on  $\beta$  of (6.8) is unexpected. A dependence on  $\beta$  might arise if resonant nonlinear triad interactions among Rossby waves were responsible for the transfer to zonal flow, but these are unable to transfer energy from isotropic two-dimensional motions to modes with  $k_x = 0$ . Newell (1969) suggests that quartic resonances or near resonances could explain these transfers, thus maintaining a  $\beta$ -dependence in the spectrum. Danilov & Gryanik (2001) point out that in fact the zonal energy is not distributed as a uniform spectrum, but rather as a series of peaks whose amplitudes increase roughly like  $k^{-5}$ , and provide a preliminary explanation for the observed wavenumber dependence. Given all of the above, we will take the appearance of such a  $-5$  spectrum (or wavenumber dependence of the spectral peaks) as an empirical observation with a rather weak theoretical or phenomenological justification.

Thus, we will suppose an isotropic  $k^{-5/3}$  spectra at scales  $k_\beta < k < k_f$ , an anisotropic  $k^{-5}$  spectral distribution, with most energy concentrated along the zonal axis, at scales  $k_{\beta,r} < k < k_\beta$ , and negligible energy at  $k < k_{\beta,r}$ . That is,

$$\mathcal{E}(k) \simeq \begin{cases} \mathcal{C} e^{2/3} k^{-5/3}, & k_\beta < k < k_f \\ \mathcal{C}_\beta \beta^2 k^{-5}, & k_{\beta,r} < k < k_\beta, k_x = 0 \\ 0, & k < k_{\beta,r}. \end{cases} \quad (6.9)$$

We use this phenomenological picture to determine  $k_{\beta,r}$ . Note that even in the presence of  $\beta$ , (5.3) remains valid, so that the total energy is  $E = g/2r$ . This constraint

determines the lowest wavenumber which the inverse cascade may reach, just as in (5.9). Specifically, using (6.9) we set

$$\int_{k_{\beta,r}}^{\infty} \mathcal{E}(k) dk \simeq \frac{g}{2r}. \quad (6.10)$$

Because the spectra are so steep in the Rossby wave regime, the integral is dominated by contributions from its peak at the low-wavenumber end, giving

$$k_{\beta,r} \simeq \left( \frac{\mathcal{C}_\beta \beta^2 r}{2g} \right)^{1/4}. \quad (6.11)$$

A simpler derivation results if we begin with the familiar expression for the stopping scale (Rhines 1975)

$$k_{\beta,r} = (\beta U_{rms}^{-1})^{1/2}. \quad (6.12)$$

But from (5.5)  $U_{rms} = (g/r)^{1/2}$  (where we have also assumed that  $U_{rms} \gg V_{rms}$ ), and substituting this into (6.12) we obtain (6.11), albeit without the numerical constant. Note that (6.12) is an estimate for a marginally barotropically unstable jet.

Manfroi & Young (1999) predict a jet-separation scale proportional to  $r^{-1/3}$ , or equivalently,  $k_{\beta,r} \propto r^{1/3}$ . Distinguishing between  $r^{-1/3}$  and  $r^{-1/4}$  (the latter from our (6.11)) is difficult numerically due both to the small difference in exponent and to the slow equilibration of the flow in this parameter regime.

We can formally derive an anisotropic wave spectrum in the general case assuming a balance between the wave frequency (6.2) and the inverse of the eddy timescale of (3.9). The wave spectrum in this case is

$$\mathcal{A}_\beta(k) = \mathcal{C}_\beta \beta^2 k^{4-2\alpha-3\gamma}, \quad (6.13)$$

which reduces to (6.8) in the inverse cascade of TDV. In SQG we find a  $k^{-4}$  spectrum in the Rossby wave regime, also significantly steeper than the isotropic spectrum of  $k^{-2}$  relevant in that case.

The result analogous to (6.11) for the general case is

$$k_{\beta,r} \simeq \left[ \frac{2\mathcal{C}_\beta \beta^2 r}{(2\alpha + 3\gamma - 5)g} \right]^{1/(2\alpha+3\gamma-5)}. \quad (6.14)$$

The simple argument using the analogue of (6.12) is not always possible in the generalized case, because the integral constraint corresponding to (5.3) does not always give a value for the r.m.s. velocity. For example, in SQG, the generalized energy  $E = \overline{\psi \xi} / 2$  is not a velocity squared. Rather, it is the generalized enstrophy that has units of velocity squared, but its value is not constrained solely by the forcing and the drag.

Which of the scales (6.5) and (6.11) (or (6.4) and (6.14) in the general case) is relevant for the meridional transport of a passive tracer? The scale (6.11) determines a jet scale, with vanishing meridional velocity. Bartello & Holloway (1991) demonstrate that at the jet scale, zonal advection so dominates meridional advection that little meridional mixing occurs. We thus expect the scale (6.5), the largest scale of *isotropic* turbulence, to act as a mixing length, and explore this further in §7. Held & Larichev (1996) utilized the scaling (6.5), without the numerical prefactor, as a mixing length in their theory for turbulent quasi-geostrophic heat fluxes.

## 7. Numerical examinations of diffusivity scalings

We now describe sets of numerical simulations designed to test the diffusivity predictions for TDV, SQG and LQG with linear drag. We also test TDV with linear drag and  $\beta$ . Mixing lengths for each case have been derived in the previous two sections, but velocity scales have not—both are required for estimates of diffusivity given by (4.8). It is difficult to generalize the calculation of velocity variance among the various cases, so we consider this detail, and the predictions for the diffusivities themselves, in the context of each case separately.

All simulations were performed using a two-dimensional de-aliased spectral model with  $512^2$  equivalent horizontal gridpoints ( $k_{max}/k_{min} = 255$ ). A leap-frog timestep is used to advance the solution, and a weak Robert filter suppresses the computational mode. In each case, a passive tracer is advected with the calculated flow. The flow is forced with an isotropic forcing at high wavenumber, typically about  $k_f/k_{min} = 160$ . The magnitude of the generation rate is fixed at  $g = 1$ , less an amount due to small-scale dissipation (see Appendix B for details of the forcing function).

Small-scale variance in both the generalized vorticity field (i.e. enstrophy) and in the tracer field are dissipated with a highly scale-selective exponential cutoff filter ((B9) and (B10)) with vanishing dissipation below a cutoff wavenumber  $k_{cut}$ . For all simulations presented here,  $k_{cut}/k_{min} = 165$  for the advecting flow and  $k_{cut}/k_{min} = 1$  for the tracer. The exponent  $s$  in (B9) is  $s = 8$  for the advecting flow and  $s = 2$  for the tracer. For the advecting flow,  $k_{cut}$  is just larger than the forcing scale and is the scale at which we begin to allow small-scale dissipation—traditional hyperviscosity, by contrast, dissipates at all scales. The dissipation level does not become significant until near the maximum wavenumber in the computational domain. Thus, while we focus here on maintaining as wide an inverse cascade range as possible, we have allowed a reasonable direct cascade for wavenumbers  $k > k_f$ . The small-scale dissipation, despite its presence only at  $k > k_f$ , removes some of the up-scale-cascading invariant. We calculate this loss and use it to define a  $g_{eff} < g = 1$  ( $g_{eff} \simeq 0.5$  for all the simulations—see Appendix B).

In each of the following sections, we state values as non-dimensionalized using a length given by the inverse forcing scale  $L = k_f^{-1}$  and a time given by a combination of the generation rate  $g$  and forcing scale. The former has units

$$g \sim [L^{3(\gamma-1)} T^{-3}],$$

so that a non-dimensional measure of the time is

$$T = [g k_f^{3(\gamma-1)}]^{-1/3}. \quad (7.1)$$

All values with a \* superscript have been non-dimensionalized by these scales.

For each dynamical case considered, a series of simulations was performed. Each simulation described is run for several eddy turnover times after a statistically steady state is achieved; averages are taken over the equilibrated phase of a given run. Each simulation was performed with a different drag coefficient, the values of which were chosen such that the halting scales were large compared to the forcing scale, but not too close to the domain scale.

### 7.1. Two-dimensional vorticity flow with linear drag

We begin with the straightforward case of two-dimensional vorticity dynamics dissipated by linear drag, namely equations (5.2) and (2.3) with  $\alpha = 2$ . In this case  $E$  cascades up-scale with spectral slope  $\gamma = 5/3$ . Five simulations were performed in

which the drag was set to

$$r^* = r(gk_f^2)^{-1/3} = (0.86, 1.5, 2.4, 3.7, 6.0) \times 10^{-2}.$$

We predict a spectral shape given by (5.20a) and a spectral peak given by (5.23a). Since the total energy, according to (5.5), is  $E = g/2r = (U_{rms}^2 + V_{rms}^2)/2 \simeq V_{rms}^2$  (assuming isotropy), the integrated (r.m.s.) meridional velocity  $V_{rms}$  is

$$V_{rms} = \left(\frac{g}{2r}\right)^{1/2}. \quad (7.2)$$

Using (4.8), (5.23a) and (7.2), we estimate the eddy diffusivity, or integrated tracer flux, to be

$$D \simeq \left[ \left(\frac{5}{9\mathcal{C}}\right)^3 \frac{1}{2} \right]^{1/2} gr^{-2}. \quad (7.3)$$

We use  $\mathcal{C} = 6$  in numerical estimates.

Figure 2 shows the spectra of the energy, tracer variance and tracer flux, as well as the stopping scales, r.m.s. velocities and diffusivities for each simulation, along with their respective predictions. The halting scale  $k_0$  is predicted by (5.23a) with some accuracy. (A similar result is inferred from the soap-film experiments of Rivera & Wu 2000.) However, the amplitude of the predicted spectrum (5.20a) falls off much more rapidly than the experimental spectrum at small wavenumbers; the predicted spectrum evidently fails when drag is dominant. Consistently, the largest overall discrepancy between theory and simulation occurs for the simulation with the highest drag, in which case the magnitude of the predicted spectrum falls well below that obtained numerically. Neither fact is surprising, since the theoretical spectrum is derived under the assumption of significant separation between the drag and forcing scales, and is formally valid only where deviations from constant  $\varepsilon$  are small, which is not true at small wavenumbers. Both the tracer variance and flux spectra have slopes close to  $-5/3$ , as predicted by (4.4) and (4.9), respectively.

The physical-space streamfunction and tracer fields for the run with the lowest drag are shown in figure 3(a). Streamfunction, rather than vorticity, is plotted since the latter is dominated by noise from the random forcing field. The large-scale flow represented in the streamfunction is nearly structureless, but with undulations whose scale represents that of the spectral peak. The absence of coherent vortices in the flow is consistent with the good fit of the theory for the spectrum in figure 2(a). The tracer field, plotted with its mean gradient, is composed of meridionally oriented plumes, with a characteristic scale similar to that of the streamfunction. The presence of fronts and ‘sheets’ in the passive tracer field has been investigated by Constantin, Majda & Tabak (1994).

### 7.2. Surface quasi-geostrophic flow

We now present simulations of SQG flow with linear drag, i.e. equations (5.2) and (2.3) with  $\alpha = 1$ . Since  $\alpha > 0$ , the up-scale-cascading invariant has a spectral slope  $\gamma = 2$ . Five simulations were performed, differing only in the magnitude of drag, whose value was set to

$$r^* = r(gk_f^3)^{-1/3} = (0.18, 0.35, 0.72, 1.4, 2.9) \times 10^{-2},$$

respectively.

The spectral shape and peak are predicted by (5.20b) and (5.23b), respectively. Estimating the velocity in this case is less straightforward. As defined in § 3, for  $\alpha = 1$ ,

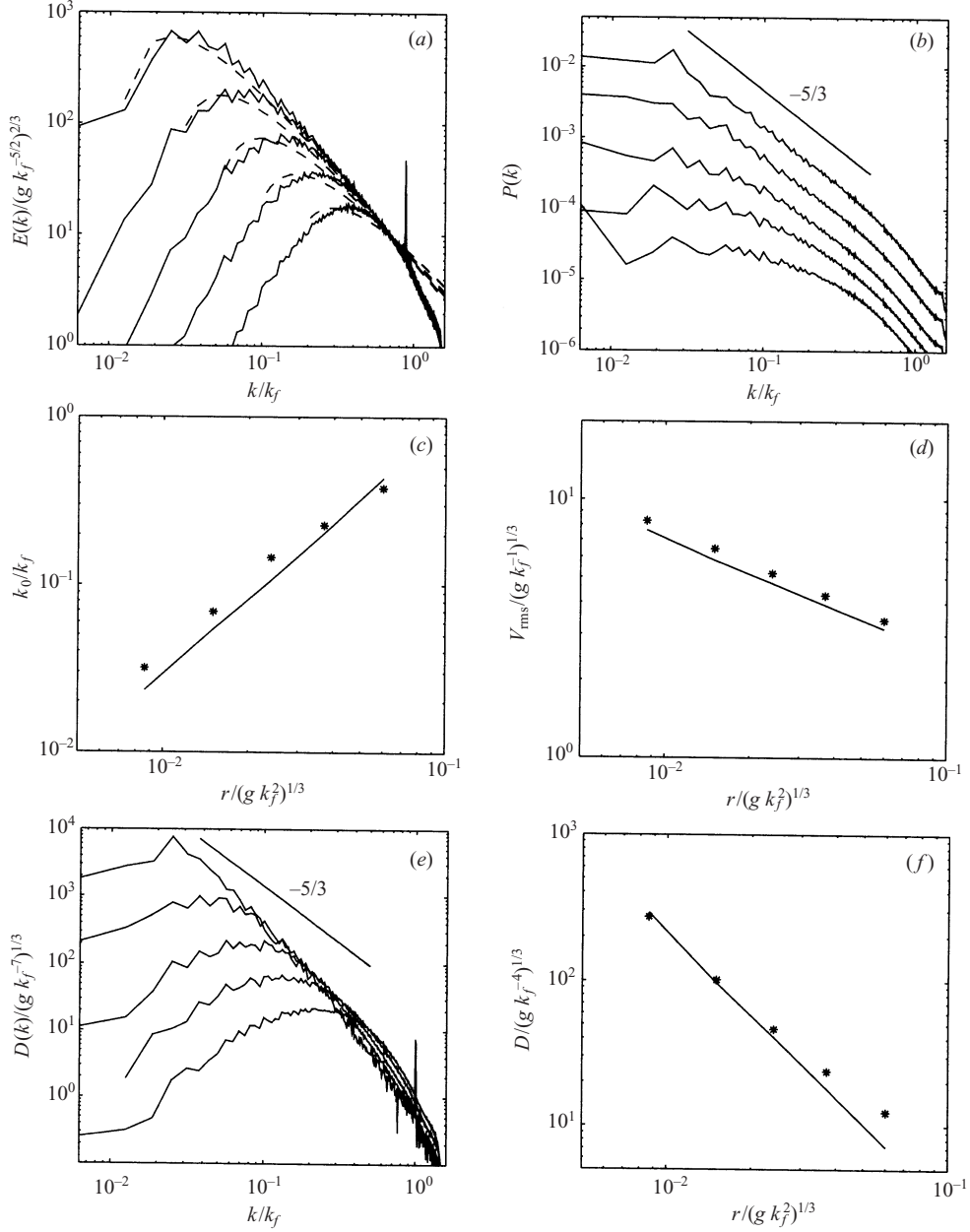


FIGURE 2. Equilibrated statistics for five simulations of TDV dynamics which differ only in the value of the drag coefficient. Values of drag used are  $r^* = (0.86, 1.5, 2.4, 3.7, 6.0) \times 10^{-2}$  and the effective generation rates are  $g_{eff} = 0.57, 0.59, 0.61, 0.64, 0.69$ . All statistics are non-dimensionalized by the timescale (7.1) and the length scale  $k_r^{-1}$ . Panels show (a) energy spectra as a function of total wavenumber (solid) and theoretical predictions (dashed) for each simulation; (b) tracer variance spectra as a function of total wavenumber for each simulation; (c) peaks of energy spectra (stars) and theoretical prediction (solid) vs. drag; (d) r.m.s. meridional eddy velocity (stars) and theoretical prediction (solid) vs. drag; (e) tracer flux spectra (the spectra of  $-v'\phi'$ ) as a function of total wavenumber for each simulation; (f) integrated tracer flux  $-\overline{v'\phi'}$  (stars) and theoretical prediction for the diffusivity (solid) vs. drag. Theoretical predictions are discussed in §7.1. In this case, the halting scale  $k_0$  is compared to the drag scale  $k_r$ .

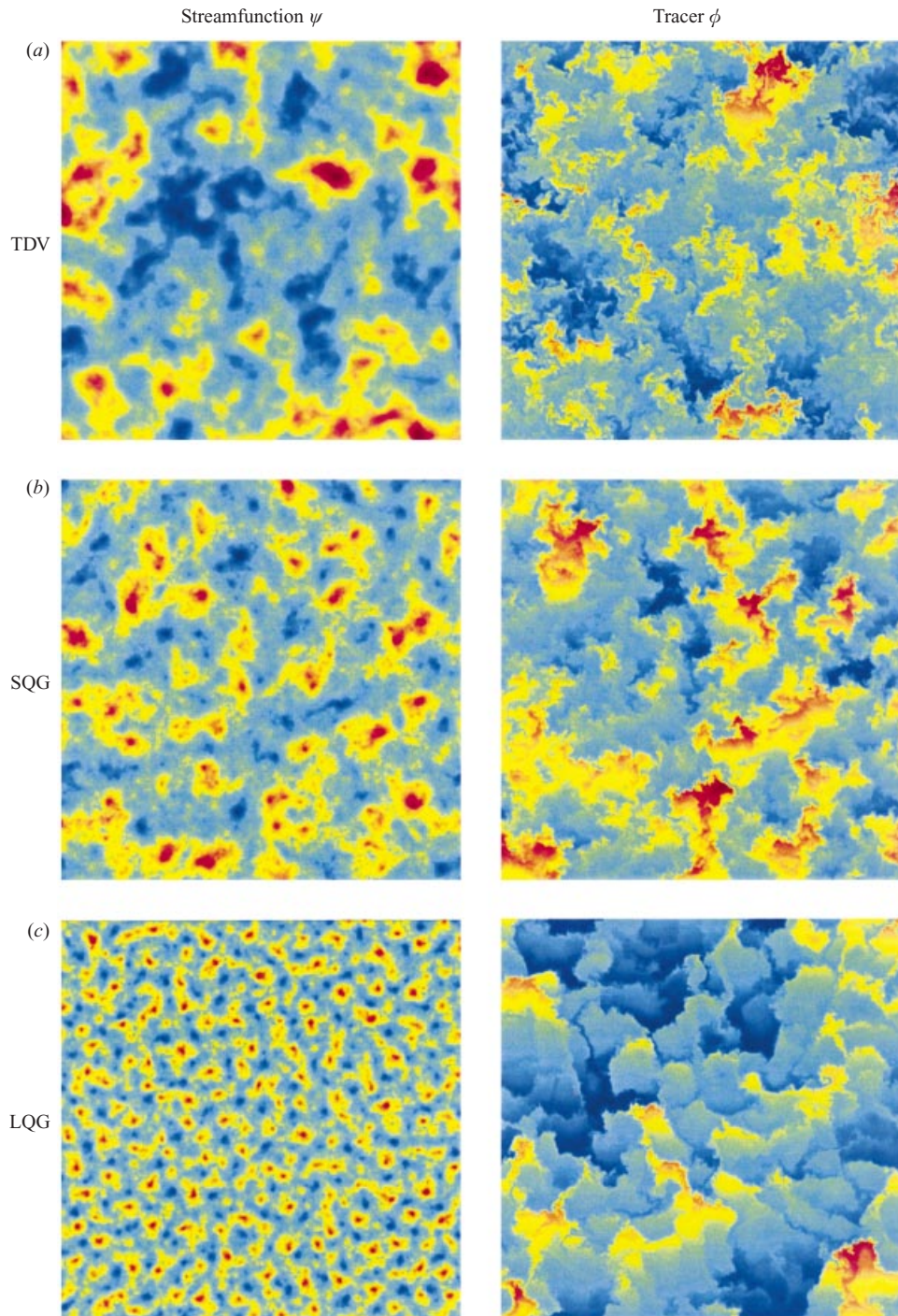


FIGURE 3. Snapshots of streamfunction (left) and tracer (right) fields for TDV (a), SQG (b) and LQG (c) simulations. Each field is taken from the equilibrated phase of the simulation with the lowest drag in each ensemble. For TDV,  $r^* = 8.6 \times 10^{-3}$ ; for SQG,  $r^* = 1.8 \times 10^{-3}$ ; for LQG,  $r^* = 3.5 \times 10^{-5}$ .

the invariants of the flow have units  $E \sim [L^3 T^{-2}]$  and  $Z \sim [L^2 T^{-2}]$ , thus in this case  $Z$  has the dimensions of energy (physically it is the temperature variance, or available potential energy). In SQG then, the r.m.s. velocity of the flow is related to the generalized enstrophy as  $Z = V_{rms}^2$  (assuming isotropy). Ignoring drag for the moment, in the inverse cascade range  $Z$  has the spectrum

$$\mathcal{Z}(k) = \mathcal{C}_E \varepsilon_E^{2/3} k^{-1}. \quad (7.4)$$

The integral of this spectrum diverges logarithmically, and we must explicitly include the forcing scale

$$Z \simeq \int_{k_c}^{k_f} \mathcal{Z}(k) dk, \quad (7.5)$$

where  $k_c$  is as given by (5.20b). We thus obtain our estimate of the r.m.s. meridional velocity scale

$$V_{rms} = [\mathcal{C}_E g^{2/3} \ln(k_f/k_c)]^{1/2}, \quad (7.6)$$

where we have taken  $g = \varepsilon_E$ .

Using (4.8), (5.23b) and (7.6), we estimate the eddy diffusivity, or integrated tracer flux, to be

$$D \simeq (g^{2/3} r^{-1}) \left[ \frac{9}{16 \mathcal{C}_E} \ln(k_f/k_c) \right]^{1/2}. \quad (7.7)$$

The spectra of  $\mathcal{E}(k)$ , the tracer variance and tracer flux, as well as the stopping scales, r.m.s. velocities and diffusivities, and their respective theoretical predictions, are plotted in figure 4. The predictions for the spectral shapes in figure 4(a) are noticeably less accurate than were the analogous curves for TDV in the previous subsection. In particular, the spectra are more shallow than the expected  $-2$  slope, even at scales which fall well inside the inverse-cascade inertial range. One might attribute this deviation from the expected slope to intermittency caused by the formation and persistence of coherent vortices in the flow. Indeed, we see evidence for such structures, but in this case one would expect the spectral slope to be steeper than its inertia-range theory prediction, when in fact it is somewhat more shallow. We offer no explanation for this behaviour at present.

We estimate the Kolmogorov constant such that the closest possible fit was achieved for all five cases, resulting in the value  $\mathcal{C} = 7.9$ . Despite the poor fits, the simulated stopping scales are fairly well predicted by the peaks of the theoretical spectral shapes. Both tracer variance and flux have the expected slopes  $-2$ . Furthermore, despite the problematic dependence of the r.m.s. velocity on the forcing scale in (7.6), the predictions made thereby are relatively accurate. The kinks in the theoretical curves for the velocities and diffusivities are due to the fact that the effective generation rate  $g_{eff}$  changed somewhat from one run to the next (see Appendix B). The diffusivity scales as anticipated, but is overestimated in magnitude by about a factor of 2.

The physical-space streamfunction and tracer fields for the run with the lowest drag are shown in figure 3(b). The structures of the flow and tracer are similar to those for TDV, but with a higher degree of localization in the streamfunction field, due to the presence of some small-scale coherent vortices in the flow. We nevertheless see patterns in the tracer field similar to those found for TDV flow in the previous subsection.

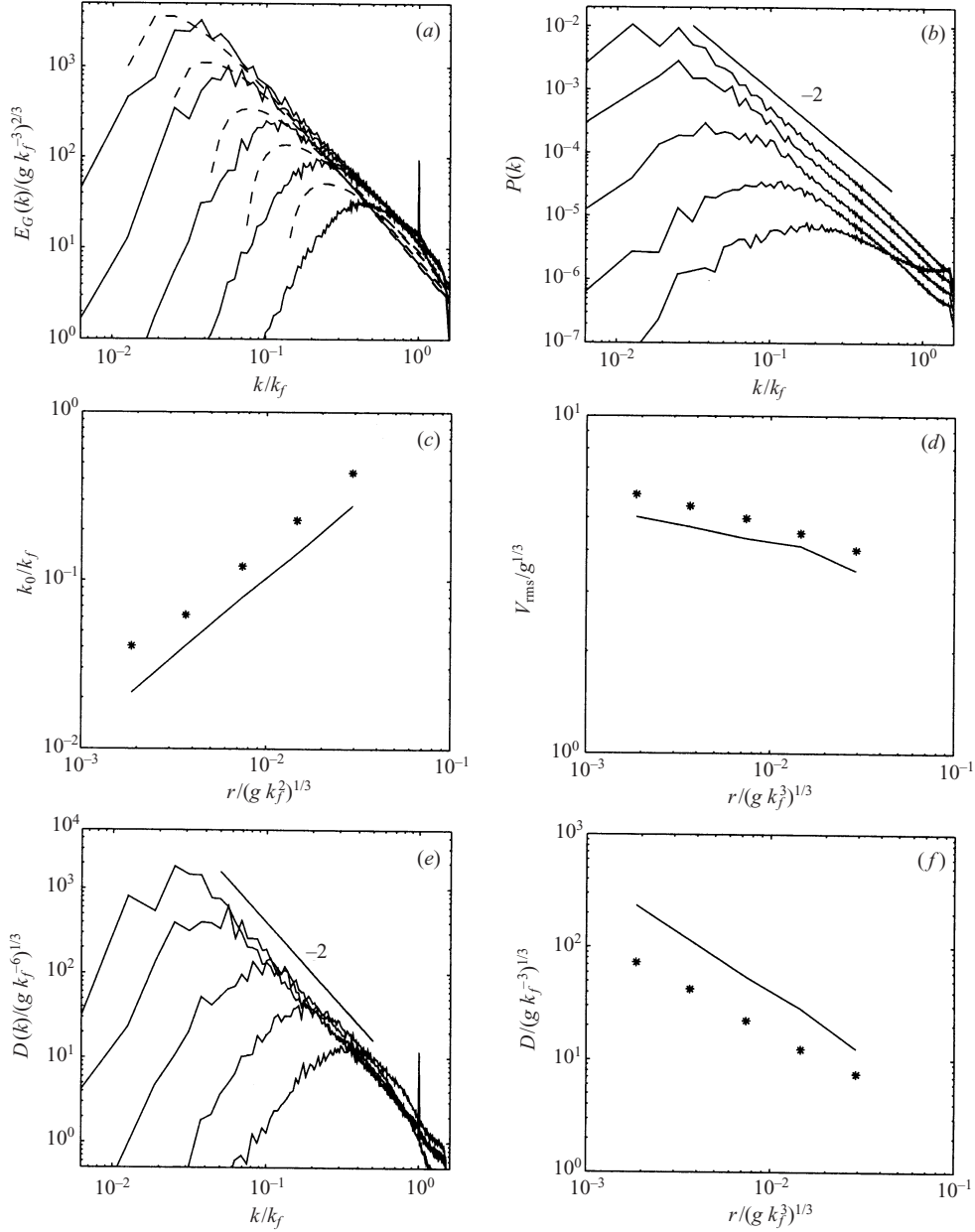


FIGURE 4. As for figure 2 but for SQG with varied linear drag. Values of drag used are  $r^* = (0.18, 0.35, 0.72, 1.4, 2.9) \times 10^{-2}$  and the effective generation rates are  $g_{eff} = 0.35, 0.37, 0.42, 0.54, 0.60$ . The theoretical predictions for the velocity and diffusivity are slightly curved due to the relatively large variations in  $g_{eff}$  between simulations. Theoretical predictions are discussed in § 7.2.

### 7.3. Large-scale quasi-geostrophic flow

Here we consider the case (5.2) with  $\alpha = -2$ , termed LQG. We actually integrate the shallow-water quasi-geostrophic equation

$$\frac{\partial q}{\partial t} + J(\psi, q) = F - rq, \quad q = (\nabla^2 - \lambda^2)\psi, \quad (7.8)$$

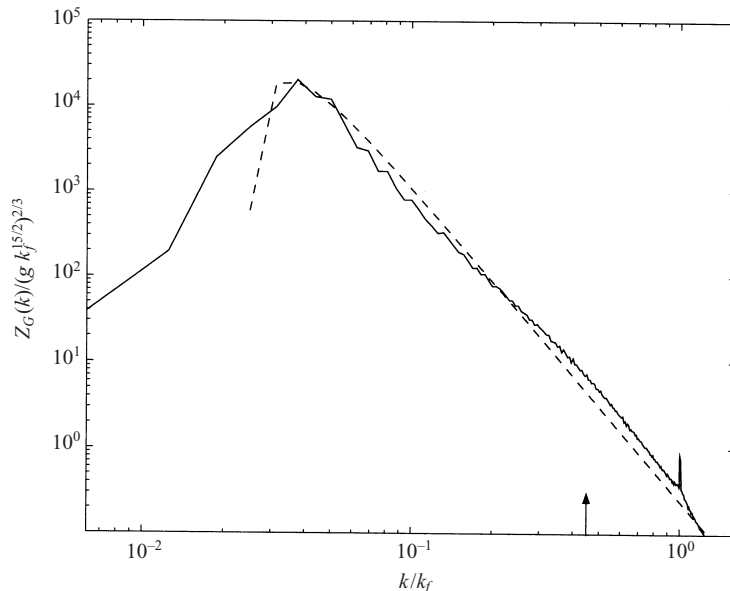


FIGURE 5. Spectra of generalized enstrophy  $|\psi|^2$  for LQG with linear drag  $r^* = 2.3 \times 10^{-4}$  (solid). Also shown is theoretical prediction (dashed). Arrow indicates location of deformation wavenumber ( $\lambda/k_f = 0.44$ ).

with  $\lambda/k_{min} = 70$ , or  $\lambda/k_f = 0.44$  so that at small wavenumbers the dynamics should be described by (5.2) with  $\alpha = -2$ . By integrating (7.8) one may see the transition from QG to LQG near scales just larger than the deformation scale (a similar approach was used by Kukharkin, Orszag & Yakhot 1995).

In the LQG regime ( $k \ll \lambda$ ), the generalized energy and enstrophy are in fact the kinetic energy (KE) and available potential energy (APE), respectively. One can see this by using the variable change (2.8) in the general expressions for the invariants (3.1), which yields

$$E_G = \frac{1}{2} \overline{\Psi \xi} = \frac{1}{2} \sum_k k^2 |\psi_k|^2 = KE, \quad (7.9)$$

and

$$Z_G = \frac{1}{2} \overline{\xi^2} = \frac{1}{2} \sum_k |\psi_k|^2 = APE/\lambda^2. \quad (7.10)$$

Since  $\alpha < 0$ , the generalized enstrophy, or APE, cascades up-scale, while the generalized energy, or KE, cascades toward small scales. Because we have chosen the deformation wavenumber  $\lambda < k_f$ , we expect a transition from the TDV-like inverse cascade at scales such that  $k \gg \lambda$  to the LQG inverse cascade at scales  $k \ll \lambda$ . Furthermore, there will be no direct cascade range for LQG in this arrangement, since the forcing scale is at smaller scale than the transition region.

In the LQG regime, from (3.8),  $\alpha = -2$  implies that for  $Z$  (the APE) the spectral slope is  $\gamma = 11/3$ . But since  $\mathcal{L}_{LQG}(k) = |\psi_k^2|$ , the spectral slope of the kinetic energy  $\mathcal{E}_{LQG}(k) = k^2 |\psi_k^2|$  is  $-5/3$ , just as it is for  $k^2 |\psi_k^2|$  in the TDV regime. Thus we expect *no change in slope* of  $k^2 |\psi_k^2|$  as we transit from TDV to LQG, but possibly a kink in the spectrum due to a possible change in the Kolmogorov constant.

In figure 5 we have plotted the spectrum of  $\mathcal{L}(k)$  for the run with the smallest drag, along with the theoretical prediction described below. Notice that at scales just

larger than the deformation scale (indicated by the arrow), the spectrum slumps but maintains a similar slope, rising slightly near the spectral peak. Because of the limited extent of the inertial range, an accurate determination of the appropriate Kolmogorov constant is not possible, and we use the value from TDV,  $\mathcal{C} = 6$ .

We expect the spectrum of generalized enstrophy to follow (5.20c) and the peak of this spectrum to be given by (5.23c). These expressions refer to the LQG formalism as derived in §3, in which  $g$  is the generation rate of the generalized enstrophy. Dimensionally  $g \sim [L^8 \tau^{-3}]$ , where  $\tau$  is the rescaled time coordinate (see equation (2.7)). Thus in terms of unscaled time,  $\tilde{g} = \lambda^6 g$ , hence

$$k_c = (\mathcal{C}/4)^{3/8} (r^3 \lambda^6 \tilde{g}^{-1})^{1/8}, \quad (7.11)$$

and

$$k_r = (27\mathcal{C}/44)^{3/8} (r^3 \lambda^6 \tilde{g}^{-1})^{1/8}, \quad (7.12)$$

where  $\tilde{g}$  is the familiar energy generation rate (the rate we set to unity in the numerical model). Since the spectral density has units  $\mathcal{Z} \sim [L^9 \tau^{-2}]$ , we can also define a spectral density in unscaled time,  $\tilde{\mathcal{Z}} = \lambda^4 \mathcal{Z}$ . But  $\tilde{g}^{2/3} = \lambda^4 g^{2/3}$  as well, so that the factors of  $\lambda$  in the unscaled spectra only appear inside the expression for  $k_c$  and  $k_r$ . Finally, though,  $\mathcal{Z}$  is a spectrum of  $|\psi|^2/2$ , so the APE spectrum is expected to be

$$\mathcal{A}\mathcal{P}\mathcal{E}(k) = \mathcal{C} \lambda^2 \tilde{g}^{2/3} k^{-11/3} [1 - (k_c/k)^{8/3}]^2, \quad (7.13)$$

with  $k_c$  given by (7.11).

From (7.9), the spectrum of kinetic energy is the spectrum of  $\mathcal{E}(k) = k^2 \mathcal{Z}(k)$ , so the total KE can be estimated

$$KE = \int_{k_r}^{\infty} k^2 \mathcal{Z}(k) dk. \quad (7.14)$$

The r.m.s. eddy meridional velocity  $V_{rms}^2 = KE$  (assuming isotropy) is thus predicted to be

$$V_{rms} \simeq \left( \frac{33C^3}{4} \frac{\tilde{g}^3}{r\lambda^2} \right)^{1/8}. \quad (7.15)$$

Following (4.8) the diffusivity of the tracer is then

$$D \simeq \left( \frac{22}{9} \frac{\tilde{g}}{r\lambda^2} \right)^{1/2}. \quad (7.16)$$

Four simulations were performed, differing only in the value of the linear drag coefficient. The non-dimensional values used were

$$r^* = r(gk_f^8)^{-1/3} = r\lambda^2(\tilde{g}k_f^8)^{-1/3} = (0.035, 0.23, 1.4, 8.9) \times 10^{-3}.$$

The spectra of APE, tracer variance and tracer flux, and the stopping scales, r.m.s. velocities and diffusivities, along with their respective theoretical predictions, are plotted in figure 6. At the largest scales, under which the assumptions used to derive LQG are most accurate, our theory predicts the spectral shape quite well. The tracer spectra are more complicated, but still roughly follow their expected slopes of  $-5/3$  (see discussion of LQG tracer in §4). In the case with the smallest drag, the tracer flux spectrum is actually *negative* in the transition region  $k \lesssim \lambda$ , but we offer no explanation for this behaviour. The stopping scales and r.m.s. velocities are also predicted somewhat successfully by our theory. Moreover, the divergence of simulation from theory is very slight, even when the stopping scale is on order the deformation scale. The theoretical prediction for the diffusivity scales like the

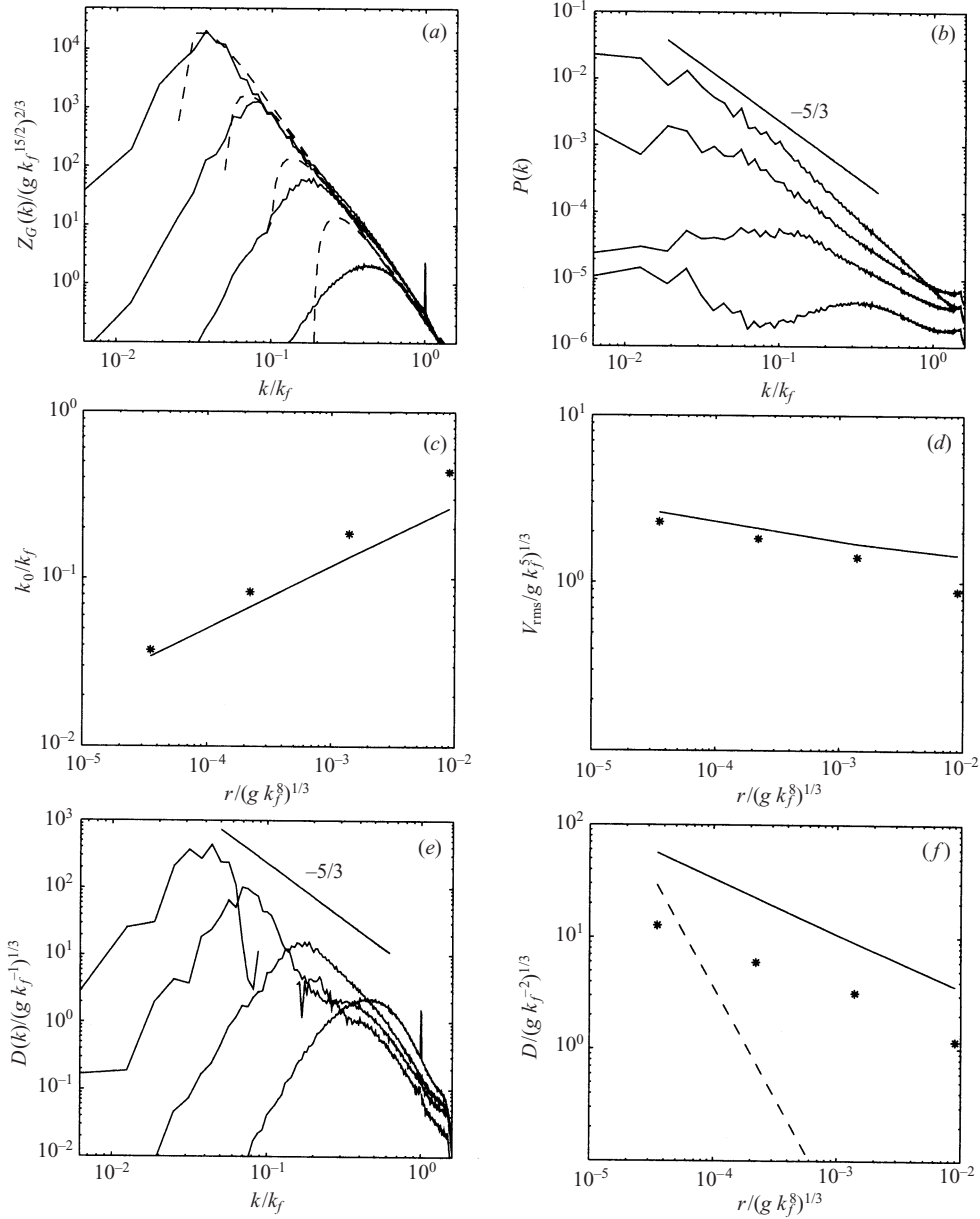


FIGURE 6. Same as figure 2 but for LQG with varied linear drag. Values of the drag coefficient used are  $r^* = (0.035, 0.23, 1.4, 8.9) \times 10^{-3}$  and the effective generation rates are  $g_{eff} = 0.57, 0.59, 0.62, 0.75$ . Theoretical predictions are discussed in § 7.3. Missing values in (e) are negative but small. Dashed line in (f) shows the prediction one would attain for TDV dynamics with the same flow parameters (see § 7.1).

simulations, but exceeds the simulated diffusivities by about a factor of 2. Also shown (the dashed line in figure 6f) is the prediction for the diffusivity from TDV with linear drag, which behaves nothing like the simulated diffusivities.

The physical-space streamfunction and tracer fields for the run with the lowest drag are shown in figure 3(c). The streamfunction is quasi-crystalline in structure,

and populated by deformation-scale vortices, as predicted by Kukharkin *et al.* (1995). This effect would presumably not be present had we simulated the strictly defined LQG equation rather than the shallow-water quasi-geostrophic equations. Despite the predominance of small-scale ordered structures in the streamfunction, and the intermittency one would presume to accompany their presence, the spectrum is well-predicted by the inertial-range theory modified for linear drag. Moreover, and perhaps more surprisingly, the tracer field is dominated by smooth plume-like structures whose characteristic scale is the *energy-containing* scale associated with the APE, rather than the deformation scale which strikes the eye in the physical-space image of the streamfunction.

There is a wealth of phenomena in these simulations which require further research to understand. The key point of the present investigation, however, has been to determine the scale responsible for the mixing of a tracer.

#### 7.4. Two-dimensional vorticity flow with linear drag and $\beta$

Lastly, we present the results of simulations of (6.1) with  $\alpha = 2$ . We have no prediction for the spectral shapes in this case, since we cannot derive a flux equation similar to (5.12) when  $\beta$  is present, but we do predict the jet scale, mixing length and r.m.s. velocity at the mixing scale (derived below). Note that now we have two independent parameters to consider:  $\beta$  and  $r$ .

In order to see the effects of  $\beta$ , drag must be set such that  $r \lesssim r_c$ , where  $r_c$  is defined by (6.7). In the simulations described here  $\beta$  is fixed such that the isotropic scale (6.5) lies within the computational domain at some relatively large wavenumber, but below the forcing wavenumber. The critical drag  $r_c$  is then fixed by  $\beta$  and the generation rate (which is fixed for all simulations described in this paper). Five values of drag are then chosen such that the largest value is just at  $r_c$  while the rest are smaller. In this way we hope to see a transition from the purely drag-induced diffusivity computed in §7.1 to the  $\beta$ -controlled diffusivity, which should be independent of drag. In particular, we choose

$$\beta^* \equiv \beta(gk_f^5)^{-1/3} = 0.73,$$

so that the inviscid  $\beta$ -scale (6.5) is (assuming a Kolmogorov constant  $\mathcal{C} = 6$  and an effective generation of  $g = g_{eff} \simeq 0.5$  – see Appendix A)  $k_\beta/k_{min} = 89$ , or

$$k_\beta/k_f \simeq 0.56.$$

The non-dimensional critical drag, according to (6.7) (using the same values for  $g$  and  $\mathcal{C}$  as above), is

$$r_c^* \simeq 9.0 \times 10^{-2}.$$

The values of drag are then chosen to be

$$r^* = (0.04, 0.43, 2.1, 4.3, 8.5) \times 10^{-2}$$

yielding predicted jet scales from (6.11) of

$$k_{\beta,r}/k_f \simeq 0.18, 0.33, 0.48, 0.58, 0.69.$$

In figure 7 we try to give a sense of these flows before showing their statistics. Figure 7(a) shows a contoured snapshot of the physical-space streamfunction for the case with the lowest drag, and demonstrates that the flow is dominated by zonal jets, as expected. The upper right panel contains the averaged two-dimensional energy spectrum for the same run. The surface height is the logarithm of the spectrum and only the smallest wavenumbers are shown. Energy is concentrated along the zonal

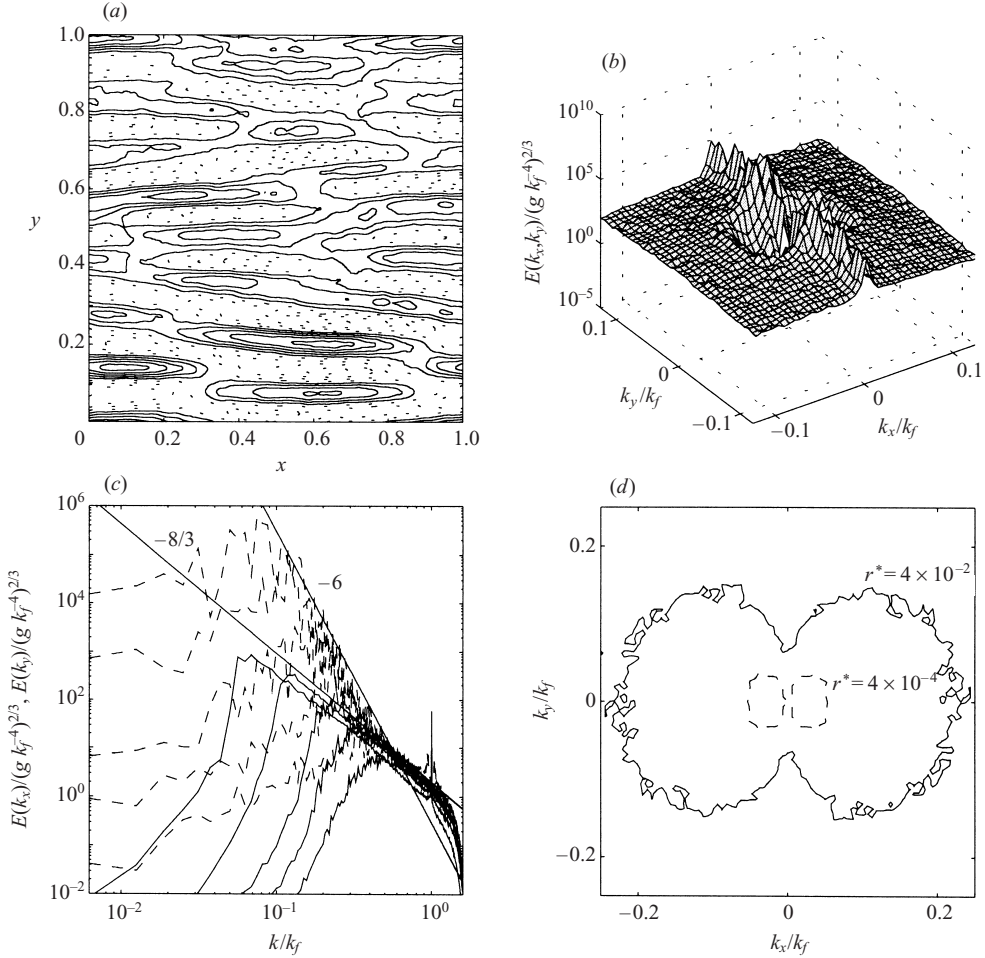


FIGURE 7. Results from simulations of TDV flow with fixed  $\beta^* = 0.73$  and varied drag. Values of drag used and effective generation rates are listed in caption of figure 8. (a) Physical-space streamfunction contours for the case with lowest drag (solid lines are positive and dashed lines are negative); (b) energy spectrum as a function of  $k_x$  and  $k_y$  for the simulation with the lowest drag (surface height is logarithmically scaled energy, and spectrum is restricted to the 20 wavenumbers in each direction closest to the origin); (c) zonal ( $k_x = 0$ ; dashed) and meridional ( $k_y = 0$ ; solid) slices of energy spectra each simulation; (d) inner-most contours at the edge of 'dumb-bell' region of spectra for simulations with  $r^* = 4.0 \times 10^{-4}$  and  $4.3 \times 10^{-2}$ .

( $k_x = 0$ ) axis, and is excluded from a dumb-bell region about  $k_x = k_y = 0$  (an argument for this shape can be found in Vallis & Maltrud 1993). Energy clearly propagates more efficiently on the zonal axis, where it is uninhibited by the  $\beta$ -effect.

Slices along the  $k_x$ - and  $k_y$ -axes of similar spectra for all five TDV runs with  $\beta$  are shown in figure 7(c). In order to compare the slopes of these spectra to our isotropic predictions, remember that integration over angle yields an integration factor  $2\pi k$ . Hence we see that the slopes of the  $k_x$  slice-spectra are about  $k^{-8/3}$ , which corresponds to an isotropic spectrum with slope  $k^{-5/3}$ , while the slopes of the  $k_y$  slice-spectra are about  $k^{-6}$ , which corresponds to an isotropic spectrum with slope  $k^{-5}$  (see equation (6.8)). Both of these slopes are as expected from arguments made and previous work noted in § 6. Furthermore, we see that all of the  $k_y$  spectra start

to steepen at the same scale (the scale at which the  $-8/3$  and  $-6$  slopes cross), approximately  $k/k_f = 0.56 \simeq k_\beta/k_f$ , as predicted. (Since  $\beta$  is held constant, this scale should be the same for all simulations.) Interestingly, energy cascades along the  $k_x$ -axis past  $k \simeq k_\beta$ , typically peaking at about the same wavenumber, but with smaller magnitude, than the corresponding  $k_y$  spectra. This phenomenon was also observed by, for example, Chekhlov *et al.* (1996) and Smith & Waleffe (1999), who point out that despite the anisotropy present at large scale, an underlying isotropic cascade still occurs.

A sense of how the two-dimensional spectrum changes as drag is increased can be gleaned from figure 7(d), which shows the inner-most contours of energy values just shy of the maximum wavenumber along the  $k_x$ -axis (so just inside the dumb-bell) for the case with the weakest drag ( $r^* = 4 \times 10^{-4}$ ) and the case with the second to largest drag ( $r^* = 4 \times 10^{-2}$ ). Despite the energy along the  $k_y$ -axis starting to steepen at a *fixed* scale for all five simulations, the dumb-bell increases in size with increasing drag coefficient.

Let us now consider the statistics of the flow. The peaks of the energy spectra along the  $k_y$ -axis correspond to the jet scales, which we expected to be described by (6.11). If the isotropic  $\beta$ -scale  $k_\beta$  is the relevant mixing length, then despite the spectrum of meridional velocity extending past  $k_\beta$ , we require the meridional velocity at the mixing scale in order to calculate the diffusivity. We estimate the turbulent meridional velocity *near the mixing scale* as

$$V_{\text{mix}} \simeq \left[ \int_{k_\beta}^{\infty} \mathcal{E}(k) dk \right]^{1/2} \simeq \left( \frac{3}{2} \right)^{1/2} \left( \frac{\mathcal{C}^3 g^2}{\beta} \right)^{1/5}. \quad (7.17)$$

Then (6.5) and (7.17) imply a diffusivity

$$D \simeq \left( \frac{3}{2} \right)^{1/2} \left( \frac{\mathcal{C}^{9/2} g^3}{\beta^4} \right)^{1/5}, \quad (7.18)$$

which is independent of  $r$ .

If, on the other hand, the jet scale  $k_{\beta,r}$  or (6.11) is the appropriate mixing length, then we expect  $D \sim r^{-1/4}$ . Moreover, at values of drag  $r \gg r_c$ , the diffusivity should roll over to the slope predicted for TDV dynamics with linear drag and no  $\beta$ , namely  $D \sim r^{-2}$ .

In figure 8 we plot the energy spectra, tracer variance and tracer flux as functions of total wavenumber, and the jet scales (peaks along  $k_y$ -axis), r.m.s. meridional eddy velocities and integrated tracer fluxes, for the five simulations. The total energy spectra show a break at a wavenumber slightly larger than  $k_\beta$ , where the spectra along the  $k_y$ -axis begin to steepen. The shape of these spectra can be best understood by referring back to figure 7(c) – the contribution to the spectra in the region with slope  $-5$  is almost solely due to zonal energy. Strikingly, there is no significant tracer flux at scales larger than  $k_\beta$  – the spectra of the diffusivity (or tracer flux) vary only slightly as drag is varied, but are essentially peaked at  $k_\beta$ . This supports our hypothesis that  $k_\beta$  is the relevant meridional mixing length.

We also plot some predictions for the jet scales, r.m.s. velocities and diffusivities. The jet-scale is slightly over-predicted by  $k_{\beta,r}$ , but for the small-drag runs, the slope is close to  $r^{1/4}$ , as predicted by (6.11). At values of drag approaching  $r_c$ , the slope of jet scale steepens. The meridional eddy velocity is somewhat flat at smaller values of  $r$ , but gently curves over the entire range. The fact that the spectrum along the  $k_y = 0$

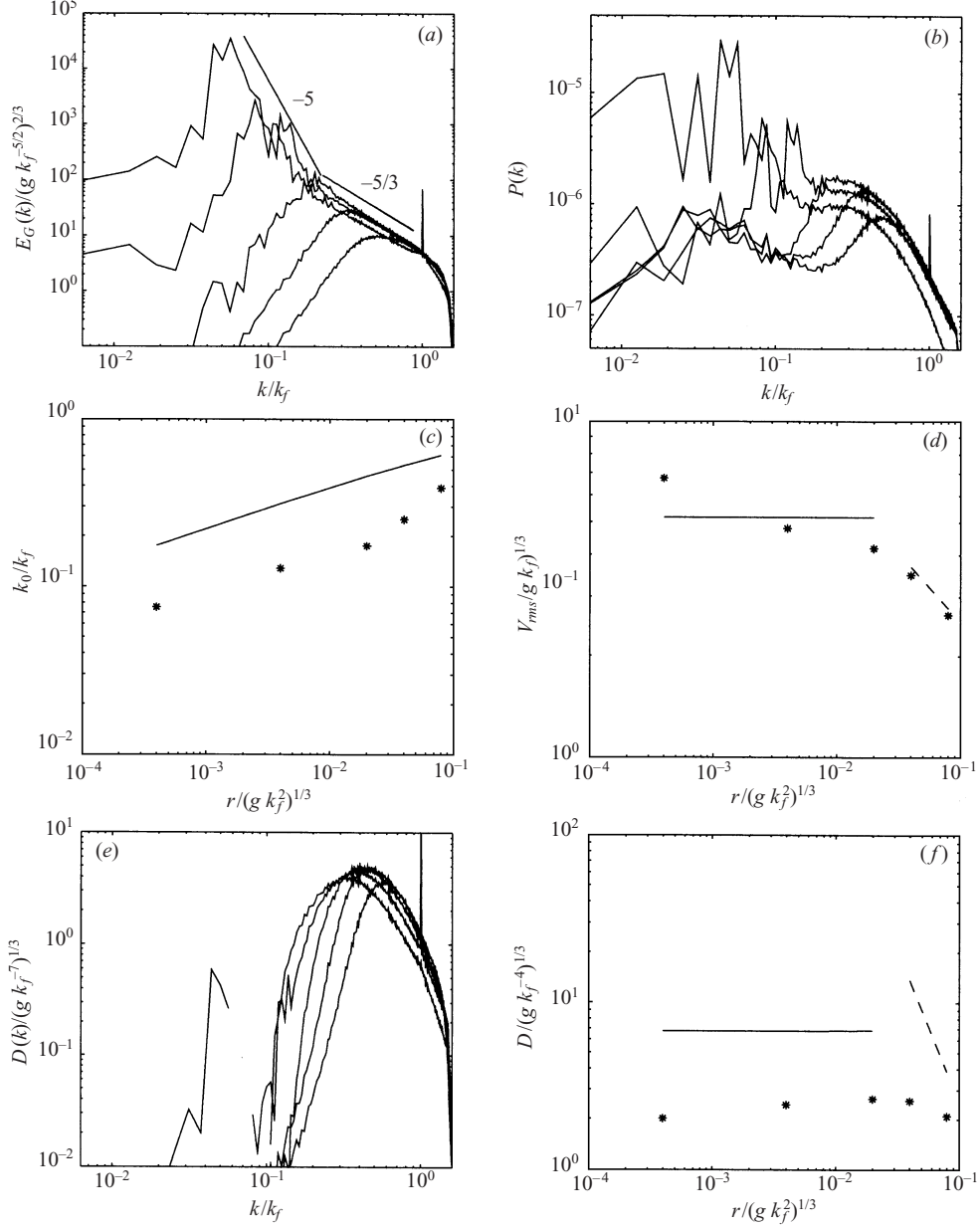


FIGURE 8. Same as figure 2 but TDV flow with varied drag and fixed  $\beta^* = 0.73$ . Values of drag used are  $r^* = (0.040, 0.43, 2.1, 4.3, 8.5) \times 10^{-2}$ , and the critical drag of (6.7) is  $r_c^* = 9.0 \times 10^{-2}$ . The effective generation rates are  $g_{eff} = 0.35, 0.37, 0.42, 0.54, 0.60$ . Theoretical predictions are discussed in § 7.4. Missing values in (e) are negative but small. Dashed lines in (d) and (f) represent predictions for large-drag,  $\beta = 0$  limit.

axis increases beyond  $k_\beta$  in figure 7 seems to be reflected in the fact that  $\overline{v^2}$  increases even at the smallest drags examined.

Finally the diffusivity of the tracer, while being quite different in magnitude, shows the expected trend: it is approximately constant for small  $r$ , then decreases for  $r \sim r_c$ . A diffusivity proportional to  $r^{-1/4}$ , which would increase by a factor of 4 over the

range of  $r$  examined, is not seen, despite the fact that  $\overline{v^2}$  continues to increase slowly with decreasing  $r$ . In fact, the diffusivity decreases slightly with decreasing  $r$  for the smallest values examined. This implies that in the small-drag limit, the inviscid, isotropic  $\beta$ -scale  $k_\beta$  of (6.5), independent of drag, is a reasonable approximation to the mixing length for the diffusivity estimate. However, these estimates are clearly not as accurate in this anisotropic problem, where more sophisticated closures (e.g. resonant interaction theory) may help in obtaining quantitatively better fits.

## 8. Conclusion

This paper has been concerned with the inverse cascade in geostrophic turbulence, and with the transport of a passive scalar by that turbulent fluid. We considered conventional two-dimensional (vorticity) dynamics, surface quasi-geostrophic dynamics, and large-scale quasi-geostrophic dynamics with a finite deformation radius.

We first showed that, for a general vorticity–streamfunction spectral field relationship of the form  $\xi_k = -k^\alpha \psi$ , we may indeed expect forward and inverse cascades of a generalized enstrophy and energy. In this context enstrophy refers to the variance of the advected field, and energy refers to the variance of the associated velocity. If  $\alpha > 0$  ( $\alpha < 0$ ) then generalized energy will cascade to larger (smaller) scale and generalized enstrophy to smaller (larger) scale. (The precise form of this statement is given in equations (A 9) and (A 10).) One notable aspect of this result is that, if  $\alpha < 0$  as for example in large-scale geostrophic turbulence, the variance of the advected field is transferred to larger scales, in contrast to the usual passive-scalar-like behaviour of a cascade to smaller scales.

Given the cascade directions, we can apply classical phenomenology to obtain predictions of the spectral slope in each inertial range, the halting scale of the inverse cascade and, at a rather less-well-founded level, a prediction for a spectrum in the inverse cascade that includes a frictional decay at small wavenumbers. The inverse cascades will be modified and made anisotropic by the presence of a mean gradient of the advected quantity—the natural generalization of the familiar  $\beta$ -effect in TDV. However, because  $\beta$  cannot alter the overall energy level in barotropic flow, the inverse cascade will only be halted by friction. (This situation should be contrasted with the baroclinic case, in which eddy energies are a highly sensitive function of  $\beta$  because of the feedback between the energy injection rate and the mixing length—see, e.g. Held & Larichev 1996.) The anisotropy of the inverse cascade leads to two distinct length scales: a wavenumber (e.g. (6.11)) characterizing the scale of zonal flow, and a smaller scale (e.g. (6.5)) that characterizes the mixing length in the meridional direction.

From these predictions we construct estimates of the diffusion coefficient of a passive tracer field stirred by the turbulent fluid and whose variance is maintained by a fixed meridional gradient. The expected dependences for the cases in which only linear drag is present are

$$\begin{aligned} \text{TDV: } D &\sim r^{-2}, \\ \text{SQG: } D &\sim r^{-1} \ln^{1/2}(k_f/k_c), \quad k_c = (2\mathcal{C}/3)(r^3 g^{-1})^{1/3}, \\ \text{LQG: } D &\sim r^{-1/2}, \end{aligned}$$

and, in the small-drag limit when  $\beta$  is present,

$$\begin{aligned} \text{TDV: } D &\sim \beta^{-4/5}, \\ \text{SQG: } D &\sim \beta^{-1} \ln^{1/2}(k_f/k_\beta), \quad k_\beta = \beta \mathcal{C}^{-1/2} g^{-1/3}. \end{aligned}$$

The last of these follows from using (6.4) for SQG as the mixing length, but was not derived nor tested here; the LQG case is special and we do not predict its diffusive behaviour in the presence of  $\beta$ , notwithstanding its probable relevance to geophysical flows. (See Kukharkin & Orszag 1996 for some treatment of this case.)

In each case in which linear drag halts the cascade, the diffusivity decreases with increasing drag coefficient. This is perhaps not immediately obvious, since, from the perspective of Brownian motion for example, damping can act to increase the irreversibility of the flow for a given eddy energy. In turbulent inverse cascades, however, decreasing drag allows for increasing eddy scales, thus increasing the eddy mixing length, and thereby increasing the diffusivity. On the other hand, when  $\beta$  is significant relative to the drag (i.e. when  $r < r_c$  in (6.6) or (6.7)), a diffusivity which is increasing or constant with drag is reasonable. In this less-turbulent, more-wave-dominated parameter regime, zonal jets act as mixing barriers, and the underlying flow is less irreversible. In this case, understanding and predicting the transport of tracer probably requires a different type of mathematical machinery than employed here.

We have tested many of these predictions numerically. Overall, the predictions for the halting scale of the inverse cascade, and the velocity amplitude at the halting scale, are quantitatively well-satisfied. We saw little evidence of non-universal behaviour over a wide range of frictional parameters, providing that the inertial range was well-developed and that the halting scale was substantially smaller than the domain scale, with no pile up of energy at the halting scale. If any of these are not satisfied the predictions may fail. (Note also that all of our simulations utilized a single type of forcing, namely a random stirring localized in wavenumber.) The form of the predicted spectrum is less well-satisfied by the numerical simulations—the latter typically falling off much less rapidly than the former at small, frictionally dominated wavenumbers. However, because the flow in this low-wavenumber regime has little energy, it does not contribute to the meridional flux of the tracer.

Consistent with these results, the transport of a passive scalar advected by the turbulent flow is down-gradient diffusive, with a diffusion coefficient well-estimated by turbulence phenomenology. In particular, for an isotropic inverse cascade, the diffusion coefficient is proportional to the product of the mixing length and the r.m.s. velocity amplitude, which are both determined by the halting scale of the inverse cascade. In the presence of a  $\beta$ -effect, the inverse cascade can develop significant anisotropy; the mixing length appropriate to the meridional transport of a passive tracer scales more or less with the isotropic  $\beta$ -scale given by (6.5), whereas the energy-containing scale is the jet scale (6.11).

Our predictions of the diffusion coefficients owe their approximate success to the presence of a good scale separation between the mean gradient and the energy-containing scales, and a second scale separation between the energy-containing scale and the forcing scale, enabling a well-defined inverse cascade to occur and minimizing the effects of the forcing. Both of these conditions are formally necessary for simple scaling behaviour, but in many cases such scalings may well remain valid well into more weakly nonlinear regimes (e.g. Held & Larichev 1996). While neither scale separation is particularly well-satisfied by meridional heat transport in the Earth's atmosphere, scale separations between large-scale gradients and the internal radius of deformation are certainly significant in the Earth's mid-oceans and on the giant gas planets, and the present diffusivity predictions may be particularly useful in those arenas.

We acknowledge the contributions of A. Fournier to the tracer diffusivity calculations, and thank B. Arbic, S. Danilov, D. Gurarie, P. Kushner and G. Lapeyre for very helpful comments. S. Danilov and D. Gurarie (preprint) have independently proposed and explored the scaling (6.11).

### Appendix A. Phenomenology of cascade directions

We first define a rescaled wavenumber  $k' \equiv k^{\alpha/2}$ . In this space, the energy and enstrophy spectra are such that

$$E_G = \int \mathcal{E}'_G(k') dk', \quad (\text{A } 1a)$$

$$Z_G = \int \mathcal{Z}'_G(k') dk', \quad (\text{A } 1b)$$

where

$$\mathcal{Z}'_G(k') = k'^2 \mathcal{E}'_G(k'). \quad (\text{A } 2)$$

The centroid of the energy distribution in this space is given by

$$k'_e \equiv \frac{\int k' \mathcal{E}'_G(k') dk'}{\int \mathcal{E}'_G(k') dk'}. \quad (\text{A } 3)$$

We now suppose that there is some initial distribution of energy distributed around this wavenumber, and that turbulence acts irreversibly to broaden this distribution. That is,

$$I' = \int (k' - k'_e)^2 \mathcal{E}'_G(k') dk', \quad (\text{A } 4a)$$

$$\frac{dI'}{dt} > 0. \quad (\text{A } 4b)$$

Then, expanding (A 4a) and using (A 3),

$$I' = \int (k'^2 - k_e'^2) \mathcal{E}'_G(k') dk'. \quad (\text{A } 5)$$

Since  $dI'/dt > 0$ , and both  $\int \mathcal{E}'_G(k') dk'$  and  $\int k'^2 \mathcal{E}'_G(k') dk'$  are constant, we must have that

$$\frac{dk_e'^2}{dt} < 0. \quad (\text{A } 6)$$

This implies that

$$\frac{dk_e^z}{dt} < 0, \quad (\text{A } 7)$$

where  $k_e^z$  is a measure of the centre of the energy distribution in conventional wavenumber space, given by

$$k_e \equiv \left[ \frac{\int k^{\alpha/2} \mathcal{E}_G(k) dk}{\int \mathcal{E}_G(k) dk} \right]^{2/\alpha}. \quad (\text{A } 8)$$

From (A 7) we immediately have

$$\left. \begin{aligned} \frac{dk_e}{dt} < 0, & \quad \alpha > 0 \\ \frac{dk_e}{dt} > 0, & \quad \alpha < 0. \end{aligned} \right\} \quad (\text{A } 9)$$

It is because the mapping between the two wavenumber spaces is monotonic that a monotonic direction of energy or enstrophy transfer in the new wavenumber space corresponds to a monotonic transfer in the true wavenumber space, although the rates of transfer (and the direction of transfer if  $\alpha < 0$ ) will differ.

Finally, we note that in the above derivations we may substitute  $\mathcal{L}_G(k)$  for  $\mathcal{E}_G(k)$ , and  $\alpha \rightarrow -\alpha$ , in equations (A 8) onward. We then readily obtain the direction of the generalized enstrophy transfer,

$$\left. \begin{aligned} \frac{dk_z}{dt} > 0, & \quad \alpha > 0 \\ \frac{dk_z}{dt} < 0, & \quad \alpha < 0, \end{aligned} \right\} \quad (\text{A } 10)$$

where, analogous to (A 8),

$$k_z \equiv \left[ \frac{\int k^{\alpha/2} \mathcal{L}_G(k) dk}{\int \mathcal{L}_G(k) dk} \right]^{2/\alpha}. \quad (\text{A } 11)$$

For TDV and SQG the generalized enstrophy, corresponding to the square of the advected quantity, cascades to smaller scales and the energy cascades to larger scales. However, for LQG dynamics the generalized enstrophy (that is, the variance of the advected quantity) cascades to *larger* scales, and generalized energy to *smaller* scales. This occurs in spite of the fact that the equation of motion is identical to that of a passive tracer, save for the additional constraint  $\Psi = \nabla^2 \xi$ . This serves to emphasize the point that inferring cascade directions in two-dimensional vorticity dynamics by analogy to passive tracer dynamics is valid only to the extent that vorticity acts as a passive tracer. This may well be the case for small-scale vorticity, but it is not a general rule.

## Appendix B. The numerical model

### *The forcing function*

The forcing is random Markovian in time and normalized at each timestep such that  $g = 1$ . Specifically, at each wavenumber  $k$  and timestep  $n$ , we calculate an initial forcing function

$$\hat{F}_n = cF_{n-1} + (1 - c^2)^{1/2} e^{i\theta}, \quad (\text{B } 1)$$

where  $\theta$  is a random phase and  $c$  is the correlation coefficient, set to 0.99 in all cases. Since the generation rate is  $g = -\overline{\psi F}$ , in order to make  $g = 1$  the actual forcing  $F_n$  is calculated as

$$F_n = -\left(\overline{\psi \hat{F}_n}\right)^{-1} \hat{F}_n. \quad (\text{B } 2)$$

The effective forcing, however, is less than 1 due to some loss from the small-scale filter, but this loss is restricted to scales smaller than the forcing scale. We calculate this loss and find the effective generation rate via

$$g_{eff} = 1 + \langle \overline{\psi \mathcal{D}_\psi} \rangle, \quad (\text{B } 3)$$

where  $\mathcal{D}_\psi$  represents the filter dissipation and  $\langle \rangle$  means a time average. The latter term quickly reaches a steady value (usually about 0.45) in all the simulations and thus the effective rate  $g_{eff}$  is well defined.

#### The enstrophy filter and timestep

The equation of motion is stepped forward via a leap-frog step but with the enstrophy filter applied implicitly,

$$\frac{\xi^{n+1} - \xi^{n-1}}{2\delta_t} = R^n + H(k)\xi^{n+1}, \quad (\text{B } 4)$$

where  $R^n$  represents the right-hand-side terms at time step  $n$  and  $\delta_t$  is the magnitude of the timestep. Thus

$$\xi^{n+1} = (2\delta_t R^n + \xi^{n-1})F(k), \quad (\text{B } 5)$$

where

$$F(k) = [1 + 2\delta_t H(k)]^{-1} \quad (\text{B } 6)$$

is the filter.

Although we do not use it, let us, as an example, consider a hyperviscosity filter of order  $s$ , i.e.  $(-1)^{s/2+1} v_s \nabla^s \xi$ , then

$$H(k) = -v_s k^s.$$

Optimal estimates for the timestep and hyperviscosity are (see, e.g. Maltrud & Vallis 1991)

$$\delta_t \simeq \frac{2\pi}{N k_{max}^{2-\alpha} \xi_{rms}}, \quad v_s \simeq (\xi_{rms} k_{max}^{2-\alpha}) k_{max}^{-s}. \quad (\text{B } 7)$$

(This former estimate is used to calculate an adaptive timestep in the model.) Using these estimates in the hyperviscous filter then yields

$$F_{hw}(k) = \left[ 1 + \frac{4\pi}{N} \left( \frac{k}{k_{max}} \right)^s \right]^{-1}, \quad (\text{B } 8)$$

which is independent of the flow.  $N = 2k_{max}$  is the equivalent horizontal resolution. Note that  $F(0) = 1$  and  $F(k_{max}) = (1 + 4\pi/N)^{-1}$ , so that no dissipation happens on the largest scale, and the maximum dissipation is a function only of the resolution. Furthermore, and sensibly, as  $N \rightarrow \infty$ ,  $F(k_{max}) \rightarrow 1$ . Finally, the power  $s$  only affects the curvature of the filter—the higher the power, the less affected are the smaller wavenumbers (larger scales).

Loosely following LaCasce (1996, and personal communication) we construct an exponential cutoff filter with the explicit property of having absolutely no dissipation at wavenumbers smaller than some preset cutoff wavenumber,  $k_{cut}$ . In particular, suppose we choose

$$F_{ec}(k) = \begin{cases} \exp[-a(k - k_{cut})^s], & k > k_{cut} \\ 1, & k \leq k_{cut}. \end{cases} \quad (\text{B } 9)$$

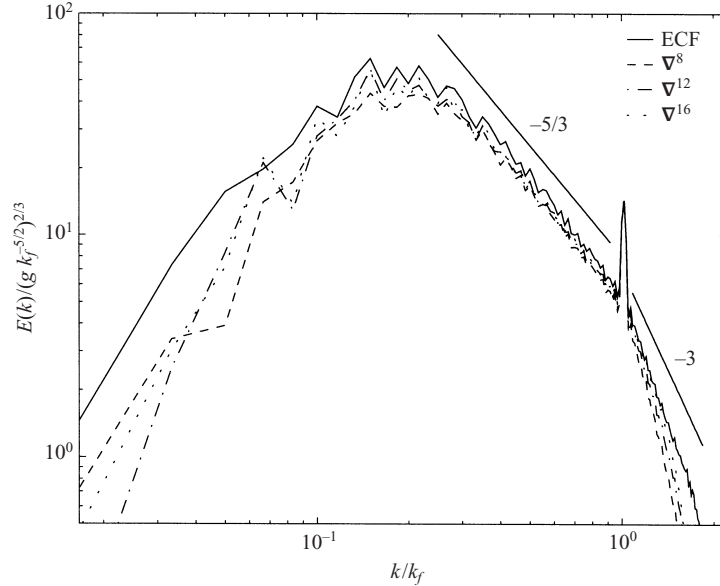


FIGURE 9. Comparison of energy spectra for TDV with various small-scale dissipation functions. Exponential cutoff filter (solid) vs.  $\nabla^8$  (dashed),  $\nabla^{12}$  (dash-dot) and  $\nabla^{16}$  (dotted) hyperviscous filters. Resolution for these runs is  $256^2$ , forcing is at  $k_f/k_{min} = 60$  and drag is  $r^* = 0.03$ . Also shown are lines representing slopes expected from simple Kolmogorov scaling. Exponential cutoff wavenumber in these simulations is  $k_{cut}/k_{min} = 70$  and the order of the filter is  $s = 8$  (see (B 9) and (B 10)).

Let us choose  $a$  such that  $F(k_{max}) = (1 + 4\pi/N)^{-1}$ , as for the optimal hyperviscous filter. Hence

$$a = \frac{\ln(1 + 4\pi/N)}{(k_{max} - k_{cut})^s}. \quad (\text{B } 10)$$

The combination of (B 9) and (B 10) gives our filter.

Comparisons of the exponential cutoff filter to the hyperviscous filters are shown for a series of TDV and tracer calculations in figure 9. The slope of energy spectra with the exponential cutoff filter at small scales is closer to the expected  $-3$  than for any order of hyperviscous filter. Also, both tracer variance and energy are higher at the largest scales with the cutoff filter.

#### REFERENCES

- ARBIC, B. K. 2000 Generation of mid-ocean eddies: the local baroclinic instability hypothesis. PhD thesis, Massachusetts Institute of Technology.
- BARTELLO, P. & HOLLOWAY, G. 1991 Passive scalar transport in  $\beta$ -plane turbulence. *J. Fluid Mech.* **223**, 521–536.
- BATCHELOR, G. K. 1953 *Theory of Homogeneous Turbulence*. Cambridge University Press.
- BORUE, V. 1994 Inverse energy cascade in stationary two-dimensional homogeneous turbulence. *Phys. Rev. Lett.* **72**, 1475–1478.
- CHEKHLOV, A., ORSZAG, S. A., SUKORIANSKY, S., GALPERIN, B. & STAROSELSKY, I. 1996 The effect of small-scale forcing on large-scale structures in two-dimensional flows. *Physica D* **98**, 321–334.
- CONSTANTIN, P., MAJDA, A. J. & TABAK, E. 1994 Formation of strong fronts in the two-dimensional quasigeostrophic thermal active scalar. *Nonlinearity* **7**, 1495–1533.

- DANILOV, S. & GRYANIK, V. 2001 Vorticity structure, jets, and spectra in quasi-stationary beta-plane turbulence with a strong zonal component. Preprint.
- DANILOV, S. D. & GURARIE, D. 2000 Quasi-two-dimensional turbulence. *Usp. Fiz. Nauk.* **170**, 921–968.
- DANILOV, S. & GURARIE, D. 2001 Nonuniversal features of forced two-dimensional turbulence in the energy range. *Phys. Rev. E* **63**, 020203:1–4.
- GALPERIN, B., SUKORIANSKY, S. & HUANG, H. P. 2001 Universal  $n^{-5}$  spectrum of zonal flows on giant planets. *Phys. Fluids* **13**, 1545–1548.
- HELD, I. M. & LARICHEV, V. D. 1996 A scaling theory for horizontally homogeneous, baroclinically unstable flow on a beta-plane. *J. Atmos. Sci.* **53**, 946–952.
- HELD, I. M., PIERREHUMBERT, R. T., GARNER, S. T. & SWANSON, K. L. 1995 Surface quasi-geostrophic dynamics. *J. Fluid Mech.* **282**, 1–20.
- HUANG, H. P., GALPERIN, B. & SUKORIANSKY, S. 2001 Anisotropic spectra in two-dimensional turbulence on the surface of a rotating sphere. *Phys. Fluids* **13**, 225–240.
- KOLMOGOROV, A. N. 1941 The local structure of turbulence in incompressible viscous fluid for very large Reynolds numbers. *Dokl. Acad. Sci. USSR* **30**, 299–303.
- KRAICHNAN, R. & MONTGOMERY, D. 1980 Two-dimensional turbulence. *Rep. Prog. Phys.* **43**, 547–619.
- KUKHARKIN, N. & ORSZAG, S. A. 1996 Generation and structure of Rossby vortices in rotating fluids. *Phys. Rev. E* **54**, 4524–4527.
- KUKHARKIN, N., ORSZAG, S. A. & YAKHOT, V. 1995 Quasicrystallization of vortices in drift-wave turbulence. *Phys. Rev. Lett.* **75**, 2486–2489.
- LACASCE, J. H. 1996 Baroclinic vortices over a sloping bottom. PhD thesis, Massachusetts Institute of Technology.
- LARICHEV, V. D. & HELD, I. M. 1995 Eddy amplitudes and fluxes in a homogeneous model of fully developed baroclinic instability. *J. Phys. Oceanogr.* **25**, 2285–2297.
- LARICHEV, V. D. & MCWILLIAMS, J. C. 1991 Weakly decaying turbulences in an equivalent-barotropic fluid. *Phys. Fluids A* **3**, 938–950.
- LEITH, C. E. 1967 Diffusion approximations for two-dimensional turbulence. *Phys. Fluids* **11**, 671–674.
- LILLY, D. K. 1972 Numerical simulation studies of two-dimensional turbulence. *Geophys. Astrophys. Fluid Dyn.* **3**, 289–319.
- LINDBORG, E. & ALVELIUS, K. 2000 The kinetic energy spectrum of the two-dimensional enstrophy turbulence cascade. *Phys. Fluids* **12**, 945–947.
- MALTRUD, M. E. & VALLIS, G. K. 1991 Energy spectra and coherent structures in forced two-dimensional and beta-plane turbulence. *J. Fluid Mech.* **228**, 321–342.
- MANFROI, A. J. & YOUNG, W. R. 1999 Slow evolution of zonal jets on the beta plane. *J. Atmos. Sci.* **56**, 784–800.
- NEWELL, A. C. 1969 Rossby wave packet interactions. *J. Fluid Mech.* **35**, 255–271.
- OETZEL, K. & VALLIS, G. K. 1997 Strain, vortices, and the enstrophy inertial range in two-dimensional turbulence. *Phys. Fluids* **9**, 2991–3004.
- PEDLOSKY, J. 1987 *Geophysical Fluid Dynamics*, 2nd edn. Springer.
- PIERREHUMBERT, R. T., HELD, I. M. & SWANSON, K. L. 1994 Spectra of local and nonlocal two-dimensional turbulence. *Chaos, Solitons Fractals* **4**, 1111–1116.
- RHINES, P. B. 1975 Waves and turbulence on a  $\beta$ -plane. *J. Fluid Mech.* **69**, 417–443.
- RHINES, P. B. 1977 The dynamics of unsteady currents. In *The Sea* (ed. E. A. Goldberg, I. N. McCane, J. J. O'Brien & J. H. Steele), vol. 6, pp. 189–318. J. Wiley and Sons.
- RIVERA, M. & WU, X. L. 2000 External dissipation in driven two-dimensional turbulence. *Phys. Rev. Lett.* **5**, 976–979.
- SALMON, R. 1980 Baroclinic instability and geostrophic turbulence. *Geophys. Astrophys. Fluid Dyn.* **10**, 25–52.
- SCHORGHOFER, N. 2000 Energy spectra of steady two-dimensional flows. *Phys. Rev. E* **61**, 6572–6577.
- SMITH, L. M. & WALEFFE, F. 1999 Transfer of energy to two-dimensional large scales in forced, rotating three-dimensional turbulence. *Phys. Fluids* **11**, 1608–1622.
- SMITH, L. M. & YAKHOT, V. 1993 Bose condensation and small-scale structure generation in a random force driven two-dimensional turbulence. *Phys. Rev. Lett.* **71**, 352–355.

- SUKORIANSKY, S., GALPERIN, B. & CHEKHLOV, A. 1999 Large scale drag representation in simulations of two-dimensional turbulence. *Phys. Fluids* **11**, 3043–3053.
- TENNEKES, H. & LUMLEY, J. L. 1994 *A First Course in Turbulence*. MIT Press.
- VALLIS, G. K. 1993 Problems and phenomenology in two-dimensional turbulence. In *Nonlinear Phenomena in Atmospheric and Oceanic Sciences* (ed. C. F. Carnevale & R. Pierrehumbert), pp. 1–25. Springer.
- VALLIS, G. K. & MALTRUD, M. E. 1993 Generation of mean flows and jets on a beta plane and over topography. *J. Phys. Oceanog.* **23**, 1346–1362.